International Journal of Thermal Sciences 145 (2019) 106022

Contents lists available at ScienceDirect

International Journal of Thermal Sciences

journal homepage: www.elsevier.com/locate/ijts

# Pseudoplastic fluid flows for different Prandtl numbers: Steady and time-dependent solutions

A. Aguirre[a], E. Castillo[a,*], M. Cruchaga[a], R. Codina[b,c], J. Baiges[b]

[a] Departamento de Ingeniería Mecánica, Universidad de Santiago de Chile, Av Libertador Bernardo O'Higgins 3363, Santiago, Chile
[b] Universitat Politècnica de Catalunya, Jordi Girona 1-3, Edifici C1, 08034, Barcelona, Spain
[c] CIMNE – Centre Internacional de Metodes Numerics en Enginyeria, Gran Capità S/N, 08034 Barcelona, Spain

ARTICLE INFO

*Keywords:*
Stabilized finite element method
Heat exchanger
High Rayleigh numbers
Natural convection
Power-law fluid
Hopf bifurcation

ABSTRACT

In this work, a variational multiscale (VMS) finite element formulation is used to approximate numerically the natural convection in square cavity with differentially heated from sidewalls problem for Newtonian and power-law fluids. The problem is characterized for going through a Hopf bifurcation when reaching high enough Rayleigh numbers, which initiates the transition between steady and time dependent behavior, however, results found in the literature are only for air Prandtl number. The presented VMS formulation is validated using existing results, and is used to study highly convective cases, to determine the flow conditions at which it becomes time dependent, and to establish new benchmark solutions for non-Newtonian fluid flows for different Pr and power-law indexes $n$. The range of solutions were found in the range $0.6 < n < 1$ and $0.01 < Pr < 1{,}000$, and the critical Rayleigh number ($Ra_c$) where Hopf bifurcations appear were identified for all cases. Obtained results have good agreement with those previously reported in the specific literature, and new data related to the heat transfer capabilities of pseudoplastic fluids and its oscillatory behavior was identified. This non-Newtonian influence of the fluid is later checked in a 3D model of a simplified heat exchanger, where the capability of pseudoplastic fluids for energy transport proved to be enhanced when compared to the Newtonian case.

## 1. Introduction

Over the past few decades, heat transfer mechanisms have been studied using simplified geometries that allow to understand the fluid dynamics and its thermal coupling [1–3]. Among those cases, the natural convection in square cavity with differentially heated from sidewalls problem has been the most common benchmark case to test new numerical methods in the approximation of convective dominant thermally coupled flows. The problem has a simple geometry; nevertheless, the flow evolves into complex fluid dynamics as the Rayleigh number increases. This is the reason why this test case has been used as the reference problem for understanding buoyancy-driven flows, which are found in a wide range of engineering applications, including building insulation, cooling devices for electronics instruments, solar energy collectors, nuclear reactor design, etc. (see Refs. [4–6] and the references therein). Because of this, the problem has been extensively studied by many authors for both Newtonian and non-Newtonian fluids.

In the Newtonian case, for air Prandtl number (Pr = 0.71), studies are very common in the literature, with very well defined solutions both in the flow dynamics as in the heat transfer associated to the problem. For this Prandtl number, the flow remains steady in a wide range of Rayleigh numbers $Ra \lesssim 1.5{\cdot}10^8$. The beginning of time dependent solutions has been defined in the range $1.7{\cdot}10^8 < Ra_c < 1.93{\cdot}10^8$ [7–12], where $Ra_c$ is defined as the critical Rayleigh number where the Hopf bifurcation occurs. For values higher than $Ra_c$, the flow turns from periodically oscillatory to aperiodically oscillatory, and then into a fully chaotic flow [8]. A detailed study of the turbulent cavity flow with aspect ratio 4 was done in Ref. [13], using direct simulation for Pr = 0.71 and Rayleigh numbers up to $Ra = 10^{10}$. In that study, a complete data set of time averaged values are presented for temperature, velocity, turbulent kinect energy and other fields of importance. It is also shown that laminar and turbulent flows can coexist given certain conditions.

In spite of the fact that studies are not commonly focused on other Prandtl numbers, they report a strong dependency on this parameter in the thermal and hydrodynamic structures of the flow [14,15] and its unsteady behavior [16]. In Ref. [17], the problem is studied up to $Ra = 10^{10}$ for Pr = 0.71, focusing on the unsteadiness of the flow past

* Corresponding author.
*E-mail addresses:* alejandro.aguirre@usach.cl (A. Aguirre), ernesto.castillode@usach.cl (E. Castillo), marcela.cruchaga@usach.cl (M. Cruchaga), ramon.codina@upc.edu (R. Codina), joan.baiges@upc.edu (J. Baiges).

https://doi.org/10.1016/j.ijthermalsci.2019.106022
Received 14 December 2018; Received in revised form 9 July 2019; Accepted 10 July 2019

the critical Rayleigh number. It is reported that the flow becomes unsteady through an aperiodicity found where the flow detaches from the walls, before it turns into a chaotic regime. In Ref. [18], the problem is studied in order to find the Rayleigh number for which the central vortex divides into smaller vortices, using a set of different Prandtl numbers. In that work, a second order Euler-Taylor-Galerkin (ETG) finite element method with a fractional step approach is used for eleven different Prandtl numbers (Pr<1), using a structured mesh of 101 × 101 cells. Steady results are reported in the range $10^4 < Ra < 10^5$, and it is found that the core vortex breaks for lower Ra as Pr increases in the studied range. In Ref. [19], a method based on the stream function-vorticity form of the Navier-Stokes equations is proposed to solve the time dependent thermally coupled problem. Solutions are reported for Pr = 0.71 in a wide range of *Ra* ($10^3 < Ra < 10^{10}$) using a 257 × 257 grid; detailed information about the time dependent flow at the critical Rayleigh number and the turbulent behavior afterwards is given.

In the numerical simulation framework of Generalized Newtonian flows, the power-law is the standard non-Newtonian model used for understanding the influence of the shear-thinning or shear-thickening behavior of the fluid in the flow patterns. In Ref. [20], stationary results are reported up to Ra = $10^6$ for Prandtl numbers in the range $10 < Pr < 10^5$. In that work, an empirical function is proposed to estimate the critical Ra that gives place to unsteady solutions, as well as a prediction of the Nusselt number Nu given a set of *n* and Pr. The correlation is proposed by doing a scaling analysis using the boundary layer sizes. It shows good agreement with numerical computations to approximate Nu, showing that it increases as *n* decreases; however, the authors could not find a convergent solution for Rayleigh numbers high enough to find unsteady results. In Ref. [21], a detailed study on the effects of Ra and *n* on the Nusselt number in the transition from steady state and transient power-law fluids is made. The problem is solved in the range $10^5 < Ra < 10^7$ for $10^2 < Pr < 10^4$ using a Finite Volume SIMPLER algorithm and a 72 × 72 mesh. In that work, all results converge to stationary solutions. However, it is found that the convection patterns become more complex as the power-law index decreases, and a correlation between the Nusselt and Rayleigh number is proposed. Again, it is shown that the Nusselt numbers increase as the power index decreases, for a fixed Rayleigh number. In Ref. [22], the phase-change evolution of different power-law fluids are studied for a binary alloy of aluminum-silicon, considering natural convection effects and evaluating the influence of the power-law index in the time required to complete solidification. In Ref. [23], the heat transfer of different non-Newtonian nanofluids that obey the power-law rheological model is studied by varying its solid volume fraction. Results were provided for $10^3 < Ra < 10^6$ on a 100 × 100 mesh, using the finite volume method, reporting an enhancement of the heat transfer rate as its solid volume fraction increases. In general, the study Hopf bifurcations is not commonly addressed outside Newtonian fluids, even in isothermal flows [24].

As for the non-Newtonian case, results are scarce and, as far as we know, no information about the Hopf bifurcation has yet been reported. Studies regarding the influence of the power-law index and the Prandtl number on the flow dynamics, and the beginning of their time dependent behavior, are not common for values Pr ≠ 0.71, even if this Prandtl number from the physical point of view is related to gases and not liquids. For this reason, we present in this work a detailed study of the influence of the rheological behavior in the fluid dynamics and heat transfer for realistic values of Prandtl numbers. On the other hand, the power-law case has been studied for moderate Rayleigh number up to Ra = $10^6$ in the range $10 < Pr < 10^5$, reporting stationary solutions only. Since highly convective flows of non-Newtonian fluids have not been deeply studied, the present work intends to be a contribution to the actual knowledge of the problem. Due to the fact that shear-thinning fluids are more common in industrial applications [25], the present work is devoted to the study of this type of fluids where, in addition, the effect of the Prandtl number in both fluid dynamics and heat transfer is evaluated in a wide range that covers from molten metals to engine oils.

This article is organized as follows. Section 2 presents the governing equations, the power-law model for non-Newtonian fluids and the Variational Multiscale (VMS) finite element formulation used to solve the problem. In Section 3, numerical results are presented for a 2D thermally coupled cavity problem using different Prandtl and Rayleigh numbers and for a 3D problem of a simplified heat exchanger using different Reynolds numbers, both considering Newtonian and non-Newtonian fluids. Conclusions are summarized in Section 4.

## 2. Incompressible thermally coupled Navier-Stokes problem

### 2.1. Problem statement

The evolutionary equations for an incompressible thermally coupled Newtonian fluid and particular cases of non-Newtonian fluids, known as Generalized Newtonian fluids [26], moving in a domain Ω of $\mathbb{R}^d$ (being $d = 2$ or $d = 3$ the space dimensions) in a time interval $[0, t_f]$, consist of finding $\boldsymbol{u}$, $p$ and $T$, such that

$$\rho\frac{\partial \boldsymbol{u}}{\partial t} + \rho\boldsymbol{u}\cdot\nabla\boldsymbol{u} - \nabla\cdot(2\eta(\boldsymbol{u})\nabla^s\boldsymbol{u}) + \nabla p = \boldsymbol{f}, \qquad \text{in } \Omega,\ t \in \left]0, t_f\right[, \tag{1}$$

$$\nabla\cdot\boldsymbol{u} = 0, \qquad \text{in} \qquad \Omega,\ t \in ]0, t_f[, \tag{2}$$

$$\rho c_p\frac{\partial T}{\partial t} + \rho c_p\boldsymbol{u}\cdot\nabla T - k\Delta T = Q, \qquad \text{in } \Omega,\ t \in ]0, t_f[, \tag{3}$$

where $\boldsymbol{u}$ is the velocity field, $p$ the pressure and $T$ the temperature field. The fluid properties are represented by $\eta(\boldsymbol{u})$, which corresponds to the apparent viscosity to be defined below, ρ the density at a reference temperature $T_{\text{ref}}$, $k$ the conductivity of the fluid (assumed constant), and $c_p$ is the specific heat. With respect to the right hand side terms, $\boldsymbol{f}$ represents the external body force vector and $Q$ a heat source term. Using the Boussinesq approximation, the buoyancy forces can be taken into account defining $\boldsymbol{f} = \rho\boldsymbol{g}\beta(T - T_{\text{ref}})$, where β represents the thermal expansion coefficient and $\boldsymbol{g}$ the gravity acceleration, whose norm will be denoted by $g$. As notation, $\nabla^s\boldsymbol{u}$ in Eq. (1) represents the symmetrical gradient of the velocity vector $\nabla^s\boldsymbol{u} = \frac{1}{2}(\nabla\boldsymbol{u} + (\nabla\boldsymbol{u})^T)$.

On regard of viscosity, non-Newtonian models can vary from simple relationships between shear-stress tensor and rate of deformation to complex irreducible constitutive models that need to be solved coupled with the Navier-Stokes equations [27,28]. The simplest one is the two parameter power-law viscosity model, which is defined in terms of the tensor $\dot{\boldsymbol{\gamma}}$: $=2\nabla^s\boldsymbol{u}$, or more specifically, of its invariant $\dot{\gamma}(\boldsymbol{u}) = \sqrt{\frac{1}{2}(\dot{\boldsymbol{\gamma}}:\dot{\boldsymbol{\gamma}})}$, as

$$\eta(\boldsymbol{u}) = m\dot{\gamma}(\boldsymbol{u})^{n-1}, \tag{4}$$

where $m$ represents the consistency index and $n$ the power-law index. A typical issue when using this model is the possibilities of zero and infinity viscosities, this is addressed by setting a parameter that depends on the consistency index that does not allow viscosity to go above $\eta = 10{,}000m$ or below $\eta = m/10{,}000$, yet this was not activated in any of the studied cases.

The dimensionless numbers that define the problem should be taken into account when using non-Newtonian fluids, then for the studied cases are defined as

$$\text{Ra} = \frac{c_p^n\rho^{n+1}g\beta\delta T H^{2n+1}}{k^n m}, \qquad \text{Re} = \frac{\rho U^{2-n}\text{H}^n}{m}, \qquad \text{Pr} = \frac{mk^{n-2}H^{2-2n}}{c_p^{n-2}\rho^{n-1}}, \tag{5}$$

being Ra the power-law Rayleigh number, Re the power-law Reynolds number, Pr the power-law Prandtl number, $\delta T$ the temperature gradient that gives place to the buoyancy forces, $H$ the characteristic length and $U$ the characteristic velocity. Note that the classical expression of the dimensionless numbers are recovered when $n = 1$ and $m = \mu$ (viscosity); for this reason the same nomenclature is used in Newtonian and

non-Newtonian cases.

The set of Eqs. (1)–(3) has to be supplemented with appropriate initial and boundary conditions defined over $\partial\Omega$, to have a well-posed system. For the sake of simplicity in the exposition, we will consider homogeneous boundary conditions $\boldsymbol{u} = 0$ and $T = 0$ over all $\partial\Omega$, and a given initial condition $\boldsymbol{u}^0$ for the velocity and $T^0$ for the temperature.

Calling $\boldsymbol{U} = [\boldsymbol{u}, p, T]$, $\boldsymbol{F} = [\boldsymbol{f}, 0, Q]$ and defining

$$\mathscr{D}_t \boldsymbol{U} = \begin{pmatrix} \rho\frac{\partial \boldsymbol{u}}{\partial t} \\ 0 \\ \rho c_p \frac{\partial T}{\partial t} \end{pmatrix}, \quad \mathscr{L}(\hat{\boldsymbol{u}}; \boldsymbol{U}) = \begin{pmatrix} \rho\hat{\boldsymbol{u}}\cdot\nabla\boldsymbol{u} - \nabla\cdot(2\eta(\boldsymbol{u})\nabla^s\boldsymbol{u}) + \nabla p \\ \nabla\cdot\boldsymbol{u} \\ \rho c_p \hat{\boldsymbol{u}}\cdot\nabla T - k\Delta T \end{pmatrix}, \tag{6}$$

we may write (1)–(3) as

$$\mathscr{D}_t \boldsymbol{U} + \mathscr{L}(\boldsymbol{u}; \boldsymbol{U}) = \boldsymbol{F},$$

where $\hat{\boldsymbol{u}}$ represents an auxiliary variable used to distinguish the velocity with the role of advection. Note that this velocity introduces the convective nonlinearity of the problem.

### 2.2. Variational form

To define the functional setting, let $H^1(\Omega)$ be the space of functions such that they and their first derivatives belongs to $L^2(\Omega)$, and let $H^1_0(\Omega)$ be the space of functions in $H^1(\Omega)$ vanishing on the boundary. Let $\mathcal{V} = (H^1_0(\Omega))^d$, $\mathscr{Q} = L^2(\Omega)/\mathbb{R}$, and $\mathscr{T} = H^1_0(\Omega)$, the spaces of the velocity, the pressure and the temperature, respectively. If we denote $\mathcal{X} := \mathcal{V} \times \mathscr{Q} \times \mathscr{T}$, the weak form of the problem consists in finding $\boldsymbol{U} = [\boldsymbol{u}, p, T]: ]0, t_f[ \to \mathcal{X}$ such that the initial conditions are satisfied and

$$\rho\left(\frac{\partial \boldsymbol{u}}{\partial t}, \boldsymbol{v}\right) + \langle\rho\boldsymbol{u}\cdot\nabla\boldsymbol{u}, \boldsymbol{v}\rangle + 2\eta(\boldsymbol{u})(\nabla^s\boldsymbol{u}, \nabla^s\boldsymbol{v}) - (p, \nabla\cdot\boldsymbol{v}) = \langle\boldsymbol{f}, \boldsymbol{v}\rangle, \tag{7}$$

$$(\nabla\cdot\boldsymbol{u}, q) = 0, \tag{8}$$

$$\rho c_p\left(\frac{\partial T}{\partial t}, \Theta\right) + \langle\rho c_p\boldsymbol{u}\cdot\nabla T, \Theta\rangle + k(\nabla T, \nabla\Theta) = \langle Q, \Theta\rangle, \tag{9}$$

for all $\boldsymbol{V} = [\boldsymbol{v}, q, \Theta] \in \mathcal{X}$, where it is assumed that $\boldsymbol{f}$ and $Q$ are such that $\langle\boldsymbol{f}, \boldsymbol{v}\rangle$ and $\langle Q, \Theta\rangle$ are well defined. In these equations and below, $\langle\cdot,\cdot\rangle_\omega$ in the integral of the product of two functions in the domain ω, with the subscript omitted when $\omega = \Omega$, and $(\cdot,\cdot)$ the $L^2(\Omega)$-inner product.

In compact form, problem (7)–(9) can be written as:

$$\rho\left(\frac{\partial \boldsymbol{u}}{\partial t}, \boldsymbol{v}\right) + \rho c_p\left(\frac{\partial T}{\partial t}, \Theta\right) + B(\boldsymbol{u}; \boldsymbol{U}, \boldsymbol{V}) = \langle\boldsymbol{f}, \boldsymbol{v}\rangle + \langle Q, \Theta\rangle, \tag{10}$$

where

$$B(\hat{\boldsymbol{u}}; \boldsymbol{U}, \boldsymbol{V}) = 2\eta(\boldsymbol{u})(\nabla^s\boldsymbol{u}, \nabla^s\boldsymbol{v}) + \langle\rho\hat{\boldsymbol{u}}\cdot\nabla\boldsymbol{u}, \boldsymbol{v}\rangle - (p, \nabla\cdot\boldsymbol{v}) + (\nabla\cdot\boldsymbol{u}, q) + \langle\rho c_p\hat{\boldsymbol{u}}\cdot\nabla T, \Theta\rangle + k(\nabla T, \nabla\Theta). \tag{11}$$

Eq. (10) needs to be complemented with initial conditions satisfied in a weak sense.

### 2.3. Galerkin finite element discretization and time discretization

Let us consider a finite element partition $\mathscr{T}_h$ of the domain Ω of diameter $h$. We will consider quasi-uniform refinements, and thus all the element diameters can be bounded above and below by constants multiplying $h$. Under the above considerations, finite element spaces $\mathcal{V}_h \subset \mathcal{V}$, $\mathscr{Q}_h \subset \mathscr{Q}$ and $\mathscr{T}_h \subset \mathscr{T}$ are constructed in the usual manner. If $\mathcal{X}_h := \mathcal{V}_h \times \mathscr{Q}_h \times \mathscr{T}_h$, and $\boldsymbol{U}_h = [\boldsymbol{u}_h, p_h, T_h]$, the Galerkin finite element approximation consists in finding $\boldsymbol{U}_h: ]0, t_f[ \to \mathcal{X}_h$ such that

$$\rho\left(\frac{\partial \boldsymbol{u}_h}{\partial t}, \boldsymbol{v}_h\right) + \rho c_p\left(\frac{\partial T_h}{\partial t}, \Theta_h\right) + B(\boldsymbol{u}_h; \boldsymbol{U}_h, \boldsymbol{V}_h) = \langle\boldsymbol{f}, \boldsymbol{v}_h\rangle + \langle Q, \Theta_h\rangle, \tag{12}$$

for all $\boldsymbol{V}_h \in \mathcal{X}_h$, and satisfying the appropriate initial conditions.

The standard option to discretize in time is the use of finite difference schemes. In particular, in this work we use both in the momentum and in the energy equation a second order backward differencing scheme, given by:

$$\frac{\partial\varphi_h^{j+1}}{\partial t} = \frac{3\varphi_h^{j+1} - 4\varphi_h^j + \varphi_h^{j-1}}{2\delta t} + \mathcal{O}(\delta t^2), \tag{13}$$

where $\delta t$ corresponds to the size of a uniform partition of the time interval $]0, t_f[$, while $\mathcal{O}(\cdot)$ represents the approximation order of the scheme. The superscript indicates the time step where the function φ is being approximated, so that $\varphi^j$ is an approximation to φ at time $t^j = j\delta t$, $j = 1,2, \ldots$.

### 2.4. Stabilized formulation

Referring to the spatial discretization, it is well known that the standard Galerkin method fails when the nonlinear convective term dominates the diffusive component. Both the momentum and the energy equations have a convection-diffusion structure and, therefore, this drawback needs to be solved. On the other hand, the discrete compatibility or inf-sup condition that restricts the use of arbitrary interpolations between velocity and pressure needs to be taken into account to have a well-posed problem with bounded pressure.

Choosing equal order approximation for velocity and pressure does not yield a stable scheme. The approach used in this work consists in using a stabilized formulation that permits any interpolation of the unknowns and ensures global stability. The stabilized method modify the discrete Galerkin formulation of the problem by adding some terms properly designed to enhance stability without upsetting accuracy. In short, a stabilized formulation consists in replacing $B$ in Eq. (12) by another bilinear form $B_h$, possibly mesh dependent. The stabilized method used in this work is based on the VMS approach introduced in Ref. [29] for the scalar convection-diffusion problem. The basic idea consists in splitting the continuous solution in two parts: the finite element component $\boldsymbol{U}_h$, which can be resolved by the finite element space, and the remainder $\tilde{\boldsymbol{U}}$, which will be called sub-grid scale, which finally, after some simplifications and mathematical manipulations, can to be written in terms of the finite element component, maintaining the number of unknowns of the problem.

We will omit the details of the derivation of the method. In the context of a thermally coupled Navier-Stokes problem, see Refs. [30–32] for a general description of the formulation. The method is stated for the problem defined by Eqs. (7) and (8). After some approximations, this method consists in finding $\boldsymbol{U}_h: ]0, t_f[ \to \mathcal{X}_h$ such that

$$\rho\left(\frac{\partial \boldsymbol{u}_h}{\partial t}, \boldsymbol{v}_h\right) + \rho c_p\left(\frac{\partial T_h}{\partial t}, \Theta_h\right) + B(\boldsymbol{u}_h; \boldsymbol{U}_h, \boldsymbol{V}_h) + \sum_K \langle\tilde{\boldsymbol{U}}, \mathscr{L}^*(\boldsymbol{u}_h; \boldsymbol{V}_h)\rangle_K = \langle\boldsymbol{f}, \boldsymbol{v}_h\rangle + \langle Q, \Theta_h\rangle, \tag{14}$$

for all $\boldsymbol{V}_h \in \mathcal{X}_h$, where $\mathscr{L}^*(\hat{\boldsymbol{u}}; \boldsymbol{V})$ is the formal adjoint of the operator (6) with $\hat{\boldsymbol{u}}$ fixed and without considering boundary conditions, which is given by

$$\mathscr{L}^*(\hat{\boldsymbol{u}}; \boldsymbol{V}) = \begin{pmatrix} -\rho\hat{\boldsymbol{u}}\cdot\nabla\boldsymbol{v} - \nabla\cdot(2\eta(\boldsymbol{u})\nabla^s\boldsymbol{v}) - \nabla q \\ -\nabla\cdot\boldsymbol{v} \\ -\rho c_p\hat{\boldsymbol{u}}\cdot\nabla\ \Theta - k\Delta\Theta \end{pmatrix}, \tag{15}$$

and $\tilde{\boldsymbol{U}}$ is the sub-grid scale, which needs to be approximated. If $\tilde{P}$ is the $L^2$-projection onto the space of sub-grid scales, the approximation we consider within each element is

$$\tilde{\boldsymbol{U}} = \alpha\tilde{P}[\boldsymbol{F} - \mathscr{D}_t\boldsymbol{U}_h - \mathscr{L}(\boldsymbol{u}_h; \boldsymbol{U}_h)] = \alpha\tilde{P}[\boldsymbol{R}], \tag{16}$$

where $\alpha$ is a matrix computed within each element and called matrix of stabilization parameters. Note that regardless of the definition of $\tilde{P}$, the sub-scale defined with Eq. (16) depends on the residual of the finite element approximation ($\boldsymbol{R}$), and therefore the methods are consistent

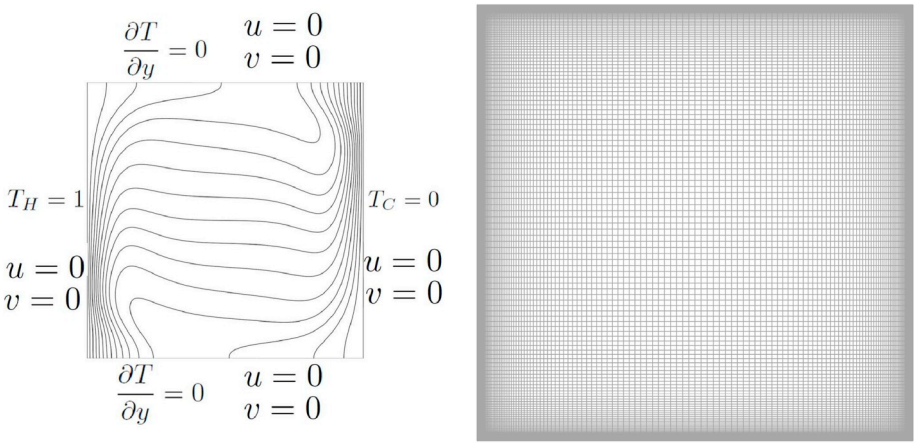


**Fig. 1.** Boundary conditions and mesh.

by construction, giving place to an optimally convergent method. This however is not a requirement of a stabilized method, and non-residual approaches can be designed, as it is explained in Refs. [33,34]. Based on [30], we define

$$\boldsymbol{\alpha} = \mathrm{diag}(\alpha_1 \boldsymbol{I}_d, \alpha_2, \alpha_3), \tag{17}$$

with $\boldsymbol{I}_d$ the identity on vectors of $\mathbb{R}^d$ and the parameters $\alpha_i$, $i = 1,2,3$, computed as

$$\alpha_1 = \left[ c_1 \frac{\eta(\boldsymbol{u}_h)}{h_1^2} + c_2 \frac{\rho|\boldsymbol{u}_h|}{h_2} \right]^{-1}, \qquad \alpha_2 = \frac{h_1^2}{c_3 \alpha_1},$$
$$\alpha_3 = \left[ c_1 \frac{k}{h_1^2} + c_2 \frac{\rho c_p |\boldsymbol{u}_h|}{h_2} \right]^{-1}, \tag{18}$$

In these expressions, $h_1$ corresponds to a characteristic element length calculated as the square root of the element area in the 2D case and the cubic root of the element volume in 3D, and $h_2$ corresponds to another characteristic length calculated as the element length in the streamline direction. The constants $c_i$, $i = 1,2,3$ are algorithmic parameters in the formulation. The values used for linear elements are $c_1 = 12$, $c_2 = 2$ and $c_3 = 4$. The stabilization parameters are computed at each integration point, and thus the physical properties to be employed in their evaluation depend on the fluid, and consequently the non-Newtonian behavior is contained in this definition.

Inserting (16), with $\boldsymbol{\alpha}$ given in (17), in (14), we get the following method: find $\boldsymbol{U}_h$: $]0, t_f[ \to \mathcal{X}_h$ such that

$$\begin{aligned} &\rho\left(\tfrac{\partial \boldsymbol{u}_h}{\partial t}, \boldsymbol{v}_h\right) + \rho c_p\left(\tfrac{\partial T_h}{\partial t}, \Theta_h\right) + B(\boldsymbol{u}_h; \boldsymbol{U}_h, \boldsymbol{V}_h) \\ &+ S_1(\boldsymbol{u}_h; \boldsymbol{U}_h, \boldsymbol{V}_h) + S_2(\boldsymbol{U}_h, \boldsymbol{V}_h) + S_3(\boldsymbol{u}_h; \boldsymbol{U}_h, \boldsymbol{V}_h) \\ &= \langle \boldsymbol{f}, \boldsymbol{v}_h \rangle + \langle Q, \Theta_h \rangle + R_1(\boldsymbol{u}_h; \boldsymbol{V}_h) + R_3(\boldsymbol{u}_h; \boldsymbol{V}_h), \end{aligned} \tag{19}$$

for all $\boldsymbol{V}_h \in \mathcal{X}_h$, where

$$\begin{aligned} S_1(\hat{\boldsymbol{u}}_h; \boldsymbol{U}_h, \boldsymbol{V}_h) = \textstyle\sum_K \alpha_1 \langle \tilde{P}\Big[ -\rho \tfrac{\partial \boldsymbol{u}_h}{\partial t} - \rho \hat{\boldsymbol{u}}_h \cdot \nabla \boldsymbol{u}_h + \nabla \cdot (2\eta(\boldsymbol{u}_h) \nabla^s \boldsymbol{u}_h) - \nabla p_h \Big], \\ - \rho \hat{\boldsymbol{u}}_h \cdot \nabla \boldsymbol{v}_h - \nabla \cdot (2\eta(\boldsymbol{u}_h) \nabla^s \boldsymbol{v}_h) - \nabla q_h \rangle_K, \\ S_2(\boldsymbol{U}_h, \boldsymbol{V}_h) = \textstyle\sum_K \alpha_2 \langle \tilde{P}[\nabla \cdot \boldsymbol{u}_h], \nabla \cdot \boldsymbol{v}_h \rangle_K, \\ S_3(\hat{\boldsymbol{u}}_h; \boldsymbol{U}_h, \boldsymbol{V}_h) = \textstyle\sum_K \alpha_3 \langle \tilde{P}\Big[ -\rho c_p \tfrac{\partial T_h}{\partial t} - \rho c_p \hat{\boldsymbol{u}}_h \cdot \nabla T_h + k \Delta T_h \Big], -\rho \hat{\boldsymbol{u}}_h \cdot \nabla \\ \Theta_h - k \Delta \Theta_h - \rangle_K, \\ R_1(\hat{\boldsymbol{u}}_h; \boldsymbol{V}_h) = \textstyle\sum_K \alpha_1 \langle \tilde{P}[\boldsymbol{f}], \rho \hat{\boldsymbol{u}}_h \cdot \nabla \boldsymbol{v}_h + \nabla \cdot (2\eta(\boldsymbol{u}_h) \nabla^s \boldsymbol{v}_h) + \nabla q_h \rangle_K, \\ R_3(\hat{\boldsymbol{u}}_h; \boldsymbol{V}_h) = \textstyle\sum_K \alpha_1 \langle \tilde{P}[Q], \rho \hat{\boldsymbol{u}}_h \cdot \nabla \Theta_h + k \Delta \Theta_h \rangle_K. \end{aligned}$$

The standard way for $\tilde{P}$ consist in taking $\tilde{P} = I$ (the identity over finite element residuals), leading to the algebraic sub-grid scale method, the option used in this work.

Eqs. (1)–(3) represent a non-linear coupled problem. The non-linearities come from both the convective nature of the momentum equation and the non-linear viscosities, which must be linearized. The same happens with the stabilization terms, which depend on the velocity. On the other hand, the thermal coupling comes from the buoyancy forces that depend on the temperature, and the convective term in the energy equation, which depends on the velocity as well. To address this, fixed point method was used to treat all the non-linearities, and the stabilization parameters and non-Newtonian viscosity are computed using the velocity from previous iteration.

Referring to the coupling between the momentum and the energy equation, a nested iterative algorithm that converges to the monolithic solution is used, which summarized in Algorithm Appendix A found in Appendix A.

## 3. Numerical results

In this section, the numerical performance of the VMS formulation presented in Subsection 2.4 is evaluated in detail in the benchmark case of natural convection in a differentially heated square cavity. Since this case is the most basic thermally coupled problem due to its simple geometry and boundary conditions, it has been frequently used to validate numerical methods over the years. At the end of this section we will present also the numerical simulation of a simplified heat exchanger.

The natural convection flow in a differentially heated square cavity problem features a $1 \times 1$ cavity, with all its sides set as no-slip walls, of which the two vertical walls are set with different temperatures $T_H$ and $T_C$, and the two horizontal walls are set as adiabatic. Fig. 1 summarizes the boundary conditions (all variables are assumed a dimensionalized). The temperature gradient between the heated walls gives rise to density differences that make the buoyancy driven flow possible. Note that according to (5), by using the characteristic length equal to one, the thermal expansion coefficient equal to one, the thermal diffusivity equal to one, density equal to one and the hot and cold wall temperatures as $T_H = 1$ and $T_C = 0$, respectively, the Rayleigh and Prandtl numbers are set as $|\mathrm{Ra}| = |\frac{g}{m}|$ and $|\mathrm{Pr}| = |m|$, respectively, for power-law fluid flows.

The mesh needs to be able to capture the velocity and temperature gradients that appear in the boundary layer in highly convective cases. For this reason the elements are exponentially concentrated near the boundaries. To check the grid dependence of the solution, three meshes of M1 = 120 × 120, M2 = 160 × 160 and M3 = 200 × 200 bilinear quadrilateral elements were tested for $\mathrm{Ra} = 10^6$, $\mathrm{Pr} = 1{,}000$ and $n = 0.6$. The velocity profiles along the horizontal and vertical centerlines are compared in order to evaluate mesh dependence, since they have high enough gradients to evaluate if the boundary layer is properly characterized. As presented in Fig. 2, the results obtained using M2 and M3 are practically overlapped and have almost unnoticeable differences

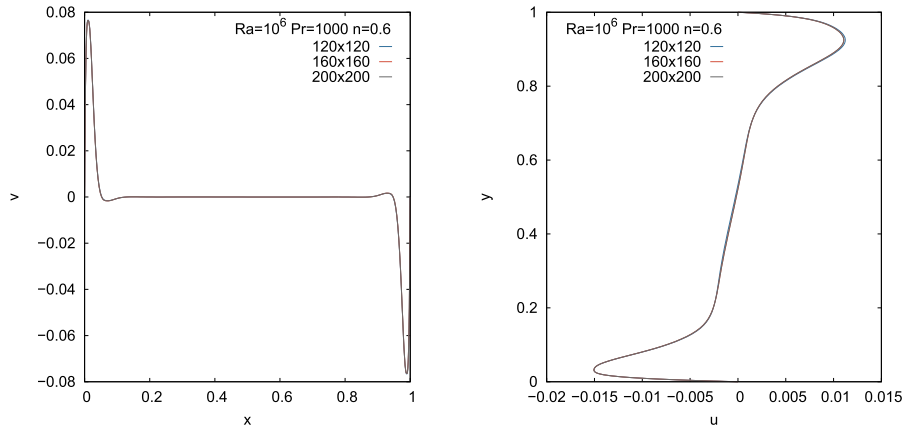


**Fig. 2.** $v$ and $u$ velocity profiles along the horizontal (left) and vertical (right) centerlines at Ra = $10^6$, Pr = 1,000 and $n$ = 0.6, using meshes M1, M2 and M3.

with M1. This would be usually enough to choose M1 above the other meshes in order to reduce computation costs; however, since higher Rayleigh number computations are certain to have greater velocity and temperature gradients, mesh M2 is used in all cases to ensure the results accuracy.

This section is subdivided in six parts: in Subsection 3.1 results are validated through comparison with results reported in the literature for Pr = 0.71 in Newtonian fluids. In Subsection 3.2, new results are presented for Pr = 0.71 for power-law fluids. In Subsections 3.3, new results are presented for power-law fluids using Pr = 0.01 and Pr = 1,000. In Subsections 3.4 and 3.5 a complete analysis regarding the unsteady solutions and heat transfer capabilities of all the studied cases is made. Lastly, a three-dimensional applied problem is presented in Subsection 3.6, where a simplified shell and tubes heat exchanger is analyzed. In this last numerical example, the enhancement of the heat transfer using shear-thinning fluids is quantified for different Reynolds numbers using the logarithmic mean temperature difference.

### 3.1. *Newtonian fluid flow at* Pr = 0.71

In this subsection, the Newtonian problem is solved for Pr = 0.71 using a time dependent approach in order to evaluate the robustness and accuracy of the VMS formulation presented in Subsection 2.4. For low and moderate Rayleigh numbers, steady state solutions are well defined; however, a Hopf bifurcation occurs in the range $1.7{\cdot}10^8 < \mathrm{Ra}_c < 1.82{\cdot}10^8$ and the flow becomes unsteady from that Ra onwards. Taking those results as a background, we start computations at Ra = $10^2$; then the solution obtained is used as initial guess to compute the Ra = $10^3$ case. By following this idea, the Rayleigh number is increased ten times between each computation until the time dependent behavior is reached. This procedure is known as the continuation method, and it is used to soften the initial transient that would develop by using non-physical initial conditions, thus saving computation time. Results are obtained up to Ra = $10^8$, whose streamlines and isotherms are presented in Fig. 3. The increase of Ra strengthens the buoyancy forces and breaks the vortex structure of the flow by dividing the initial core vortex into new vortexes that are displaced to the top left and bottom right corners of the cavity. The effect is also visible in the temperature field, as when the flow is dominated by conduction a linear temperature profile is displayed, but temperature gradients are increased as convection dominates the flow. Alongside this, a decrease of both hydrodynamic and thermal boundary layer sizes is also found. In order to validate results, Table 1 shows the Nusselt numbers obtained at the hot wall, computed as $\mathrm{Nu} = -\frac{1}{L}\int_{y=0}^{y=L}\left[\frac{L}{T_H - T_C}\frac{\partial T}{\partial x}\Big|_{x=0}\right]\mathrm{d}y$ (with $L = 1$), showing good agreement with the values found in Refs. [7,17,19,35]. Note that up to this Ra, all results reach a steady state.

By increasing the Rayleigh number further from the previous result, using again a continuation method, it is found that the flow goes through a Hopf bifurcation in the range $1.7{\cdot}10^8 < \mathrm{Ra}_c < 1.71{\cdot}10^8$, initiating an oscillatory behavior. This oscillation can be described as a slight but continuous throbbing of one or more vortexes, which can go unnoticed among the overall results. To properly illustrate this, Fig. 4 shows the results computed at Ra = $1.71{\cdot}10^8$. In this solution the global flow structure seems steady; however, there is a subtle expansion and contraction of the vortex near the top left and bottom right corners of the cavity. This is checked by plotting the velocity history at a single monitoring point inside the vortex, which describes a constant amplitude oscillation. In order to check the transition from steady to unsteady solution, a Fourier frequency spectrum (FFT) and a velocity-temperature phase diagram are plotted at the monitoring point. The analysis shows that a single and completely clean fundamental frequency is dominating the problem and the phase diagram describes a closed circular trajectory. This means that the solution presents a steady variation of both velocity and temperature. This behavior proves that the solution went through a Hopf bifurcation and will not be able to reach steady state past this Rayleigh number.

For the Ra = $1.71{\cdot}10^8$ case, a single fundamental frequency of $f$ = 6,500 of low amplitude is found, which does not present noise. This behavior is typically found in a solution that has slightly surpassed the critical Rayleigh number value. By increasing this number up to Ra = $1.82{\cdot}10^8$, as shown in Fig. 5, the fundamental frequency increases to $f$ = 6,800 and its first harmonic of $f$ = 13,600 is found in the frequency spectrum. Similar results have been presented in Ref. [19].

### 3.2. *Effect of the power-law index for* Pr = 0.71

In the previous subsection, the VMS formulation has proved to be robust enough to easily reach the Hopf bifurcation in the Newtonian case. In this subsection, it is used to study the influence of the power-law index $n$ in the flow dynamics and its time dependent behavior for a fixed Pr = 0.71.

The problem is solved for power-law indexes $n$ = 0.6, 0.8, 1.0 using the same continuation method described in subsection 3.1. It is well known that for this order of Prandtl numbers, fluid flows do not describe non-Newtonian behavior, however, since the specific literature is devoted to the value of air, we use it to validate our method. On the other hand, the choice to perform the analysis using only shear-thinning fluids is due to the fact that these fluids are the most common in the industry. Non-Newtonian cases present similar flow dynamics to the Newtonian case in conduction dominated situations (Ra ≤ $10^3$), being all characterized by the central core vortex. However, as illustrated in Figs. 6 and 7, each case evolves differently when convection dominates over conduction, and the flow development has strong dependence on the power-law index. By increasing the Rayleigh number, the core

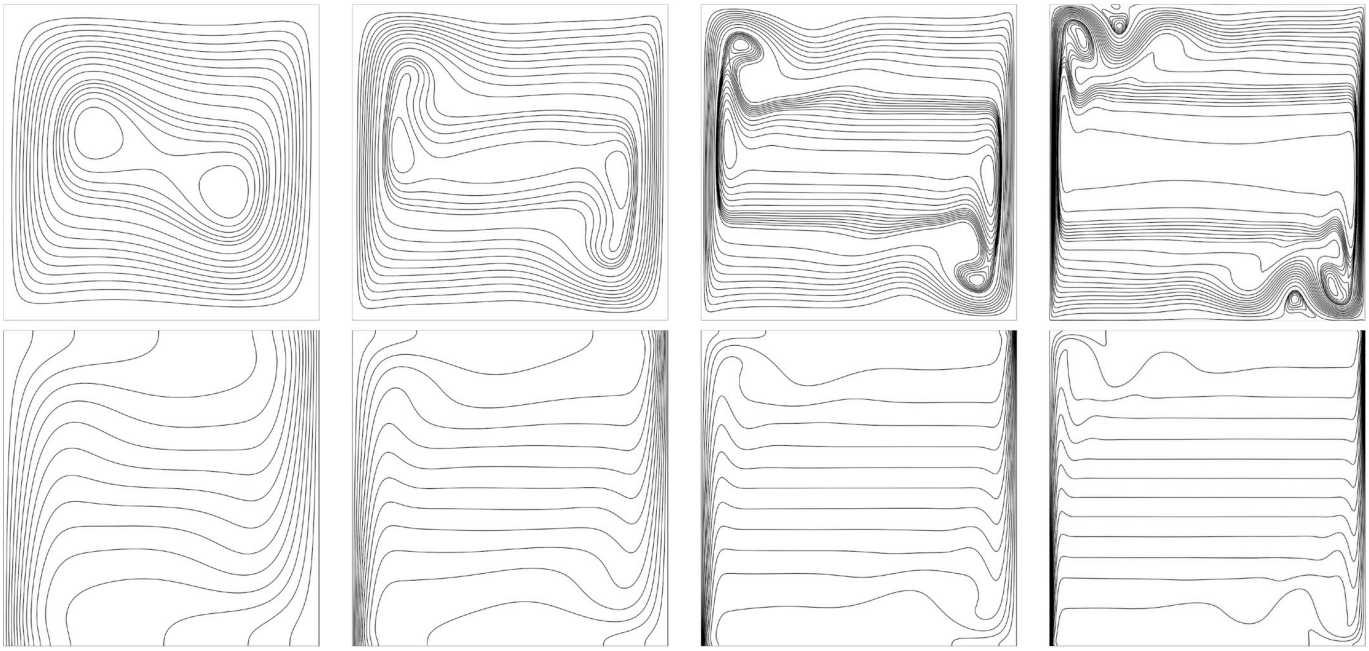

**Fig. 3.** Streamlines (top) and temperatures (bottom) for Pr = 0.71 at Ra = $10^5$, $10^6$, $10^7$ and $10^8$.

**Table 1**
Nusselt numbers for Pr = 0.71 for Ra ≤ $10^8$ at the hot wall.

| | Ra = $10^3$ | Ra = $10^4$ | Ra = $10^5$ | Ra = $10^6$ | Ra = $10^7$ | Ra = $10^8$ |
|---|---|---|---|---|---|---|
| Present | 1.1178 | 2.2450 | 4.5226 | 8.8316 | 16.5498 | 30.3345 |
| [7] | – | – | 4.521 | 8.825 | 16.522 | 30.225 |
| [17] | – | – | – | 8.817 | 16.523 | 30.225 |
| [19] | – | 2.2446 | 4.5199 | 8.8222 | 16.5187 | 30.1417 |
| [35] | – | – | – | – | 16.52 | 30.31 |
| [36] | 1.1178 | 2.2449 | 4.5214 | 8.8091 | 16.3024 | 29.9137 |

vortex breaks into two or more vortexes and, according to the results obtained, this happens for lower Ra as $n$ decreases. As illustrated in Figs. 6 and 7, this occurs at Ra ≈ $10^4$ and $10^5$ for power-law indexes 0.6 and 0.8, respectively, while it occurs at Ra ≈ $10^5$ in the Newtonian case. An important feature of this is that for shear-thinning fluids the new vortexes tend to stay close to the center of the cavity, while they move close to the vertical walls for Newtonian fluids. In a similar fashion, it was found that the isotherms are more complex as $n$ decreases, which give us the idea that shear-thinning fluids promote convective transport. Regarding the time dependent solution, it was found that the critical Rayleigh number where the Hopf bifurcation occurs decreases by lowering $n$; this agrees with the idea of the increased convective effect obtained using shear-thinning fluids. The studied cases go through Hopf bifurcations for Rayleigh numbers ranged in $2.5{\cdot}10^4 < \mathrm{Ra}_c < 2.75{\cdot}10^4$ for $n = 0.6$ and $5.5{\cdot}10^5 < \mathrm{Ra}_c < 6.5{\cdot}10^5$ for $n = 0.8$, initiating their time dependent behavior.

While it is clear that, compared to the Newtonian case, the flow develops and takes more complex structures for lower Ra on shear-thinning fluid flows, it is necessary to analyze the influence of $n$ on the velocity and thermal boundary layers. The dimensionless $v$-velocity and temperature profiles are plotted along the horizontal centerline of the cavity in Fig. 8. Compared to the Newtonian profiles, by decreasing $n$ for fixed Ra the maximum velocity increases alongside the velocity and temperature gradients, while both hydrodynamic and thermal boundary layers get thinner. Similar results were reported in Ref. [20]. On the other hand, an important characteristic of a non-Newtonian fluid flow is how the viscosity varies through the domain when velocity gradients are higher. On Fig. 9 a viscosity contour for $n = 0.6$, 0.8 and Ra = $10^4$, and a velocity-viscosity plot along the horizontal centerline of the cavity are showed. It can be clearly seen that the fluid gets thinner the lower $n$ index is, and higher velocities appear where viscosities are lower.

### 3.3. Effect of Prandtl number on power-law fluid flows

In this subsection, the influence of the Prandtl number on the flow dynamics and its time dependent behavior is analyzed. As in the previous subsection, computations have been made using the same continuation method described in 3.1. The problem has been solved for

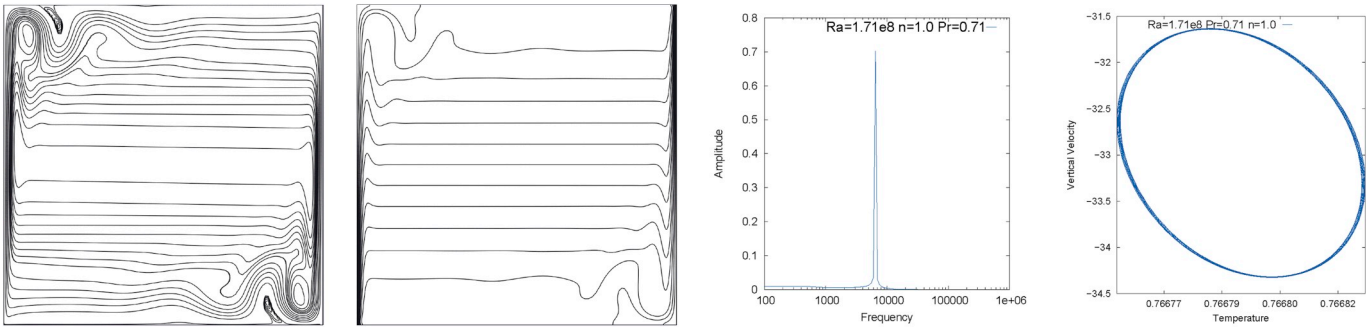


**Fig. 4.** From left to right: Streamlines and isotherms for Ra = $1.71{\cdot}10^8$, Fourier frequency spectrum and phase diagram at coordinates (0.08, 0.92).

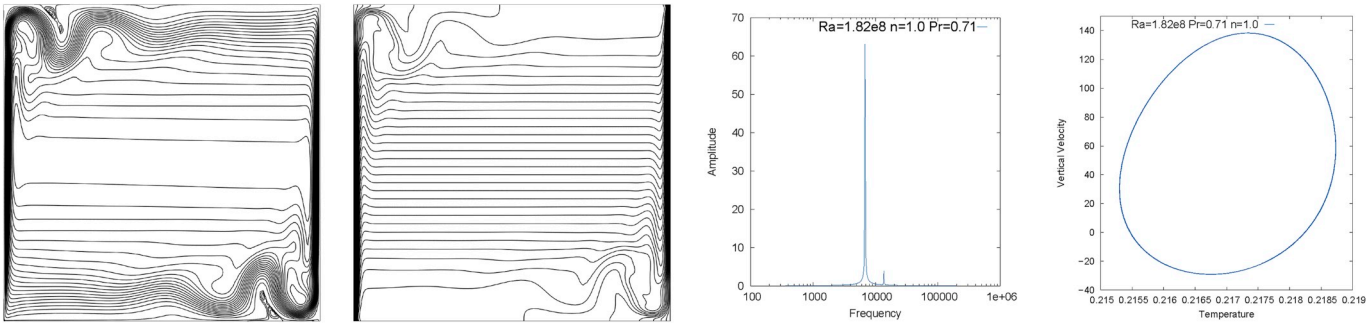


**Fig. 5.** From left to right: Streamlines and isotherms for Ra = $1.82 \cdot 10^8$, Fourier frequency spectrum and phase diagram at coordinates (0.08, 0.92).

Pr = 0.01, 10 and 1,000 for power-law indexes $n = 0.6$, 0.8 and the Newtonian case.

In the Pr = 0.01 case, the flow tends to describe a circular shape along the cavity. Figs. 10 and 11 show the flow evolution of the streamlines and isotherms for the steady solutions. As the Rayleigh number increases, small vortexes appear at the cavity corners. For this Prandtl number, the flow dynamics develop at extremely early Ra which, in the $n = 0.6$ case, where the flow goes through a Hopf bifurcation in a Rayleigh number slightly higher than the value at which secondary vortexes appear. In the other cases, the apparition of additional vortexes in the cavity corners occurs at Ra $\approx 10^3$ for $n = 0.8$ and at Ra $\approx 10^4$ for $n = 1.0$. In general, the flow becomes time dependent before the flow dynamics manages to change significantly, which means that there may be a quick change from conductive to convective transport; to verify this, however, would require further experiments.

In the opposite way, the Pr = 1,000 case is characterized by the delay of every possible development of the flow. Figs. 12 and 13, show the detail of the steady solution for increasing Ra. In this case, the vortexes get narrower and longer as Ra increases, while staying close to the vertical walls. The core vortex breaking occurs at Ra $\approx 10^4$ for $n = 0.6$, Ra $\approx 10^5$ for $n = 0.8$ and Ra $\approx 10^5$ for $n = 1.0$, and the Hopf bifurcations have been found at even higher Ra compared to the Newtonian case. Similar to the other studied cases, the hydrodynamic and thermal boundary layers become thinner, and the isotherms have a more horizontal shape as Ra increases.

To verify the influence of the Prandtl number on the flow, a comparison is made for every power-law index separately. In Fig. 14, the $v$-velocity and temperature profiles are plotted for a fixed Ra = $10^3$. This value is chosen to make a consistent comparison, since some cases become time dependent beyond this value. Both the maximum velocity and the velocity gradient increase as Pr decreases, which gives us the idea that the flow becomes more convective when this decrease happens. Nevertheless, the temperature profiles seem to be unaffected by the Prandtl number variations. The same happens when higher Ra cases are compared: as seen in Fig. 15, the temperature profiles are similar for Pr = 10 and 1,000, and only slightly different for Pr = 0.71. At this point it is safe to state that any variation of the Prandtl number has a greater effect on velocities than on temperatures, which are almost unaffected; similar results were reported in Ref. [20].

In the same way as the results showed in the Pr = 0.71 case, viscosities proven to be lower for higher velocity gradients, which result on an overall higher velocity magnitude that is specially notorious on the boundary layer. As a comparison, viscosity contours and velocity-viscosity plots are showed on Figs. 16 and 17 for Pr = 0.01 and 1,000. The shear-thinning effect increases as $n$ decreases, a notorius example is shown at the right plot of the figures, where for the same Prandtl and Rayleigh numbers, viscosity is lower and velocity magnitude is higher in the boundary layer for $n = 0.6$ compared to $n = 0.8$. Note that in the case of Pr = 1,000, the boundary layer is extremely thin due to the highly convective dynamics developed for Ra = $10^7$, and only a small section of the boundary layer is plotted.

To further validate non-Newtonian cases, the Nusselt numbers are directly compared with results found in Ref. [20] which contains steady state solutions for the Prandtl numbers used in this work. Results are plotted as function of Ra and $n$ for a fixed Pr = 1,000 in Fig. 18. The percentage difference of results goes from 1.76% in the Newtonian case for the lowest Ra to 6.7% in $n = 0.6$ for the highest Ra value, showing that obtained results are consistent with those reported in the literature.

### 3.4. Nusselt number analysis

Regarding the heat transfer capabilities of each fluid, the Nusselt number has been obtained at the hot wall of the cavity, and the new results for non-Newtonian steady solutions are summarized in Tables

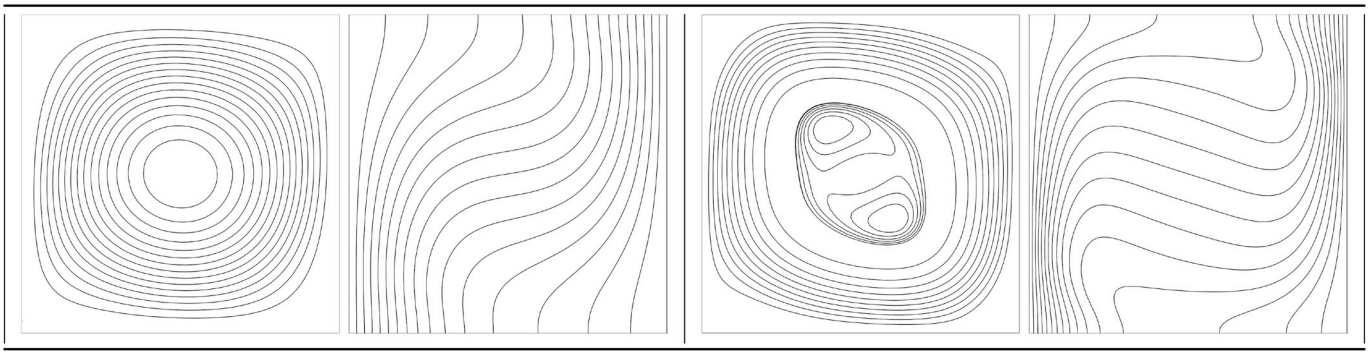

**Fig. 6.** Streamlines and isotherms for Ra = $10^3$ (left) and Ra = $10^4$ (right) using $n = 0.6$ and Pr = 0.71.

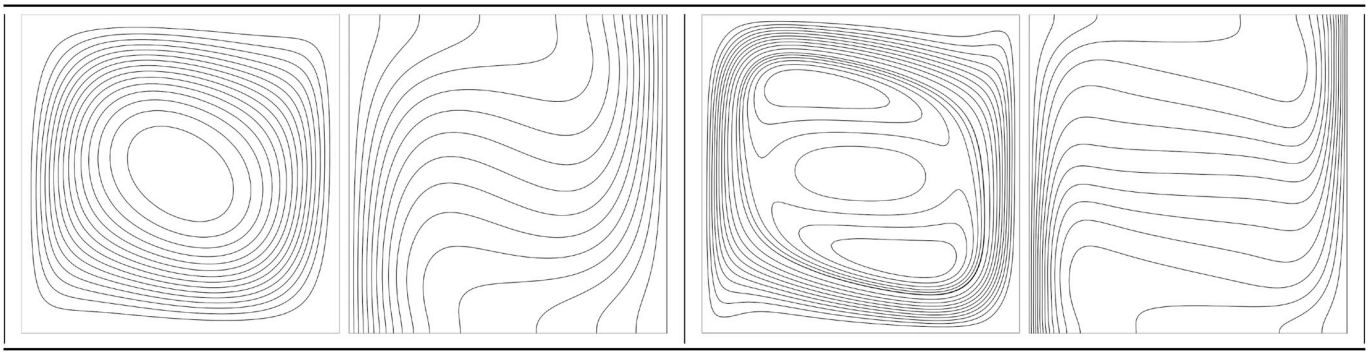

**Fig. 7.** Streamlines and isotherms for Ra = $10^4$ (left), Ra = $10^5$ (right) using $n = 0.8$ and Pr = 0.71.

2–5. Computations have been made also for Pr = 1, although the results are not included because they are similar to the Pr = 0.71 case. Note that the Nusselt number values are reported for stationary solutions only.

It is observed that by increasing Ra the Nusselt number rapidly increases for all $n$ and Pr considered; this makes sense, since the buoyancy forces get stronger than the viscous forces by increasing Ra, and thus the strength of the natural convection is increased. Another important characteristic of the flow is that any variation of Pr has a weak effect on the heat transfer capabilities; however, there is a slight decrease of Nu when decreasing Pr for fixed $n$ and Ra. Fig. 19 summarizes this behavior for all cases, where all curves are almost overlapped for any Pr number. In the other hand, the opposite happens when varying $n$, since, as proved in Subsection 3.2, it has great influence on the flow. As seen in Fig. 20, by decreasing $n$ the Nusselt number is strongly boosted for a fixed Pr, making shear-thinning fluids those with the strongest heat transfer capabilities. Note that since Nusselt numbers are plotted only in cases that reached stationary results, the number of points of each plot depends on the Pr and $n$ that is analyzed.

### 3.5. Time dependent solutions

Given the results presented in Subsections 3.2 and 3.3, it can be anticipated that the Rayleigh number for which the Hopf bifurcation occurs increases with both the Prandtl number and the power-law index. Table 6 presents the specific values that we have found of the range where the bifurcation takes place. A graphical representation of these numbers is illustrated in Fig. 21.

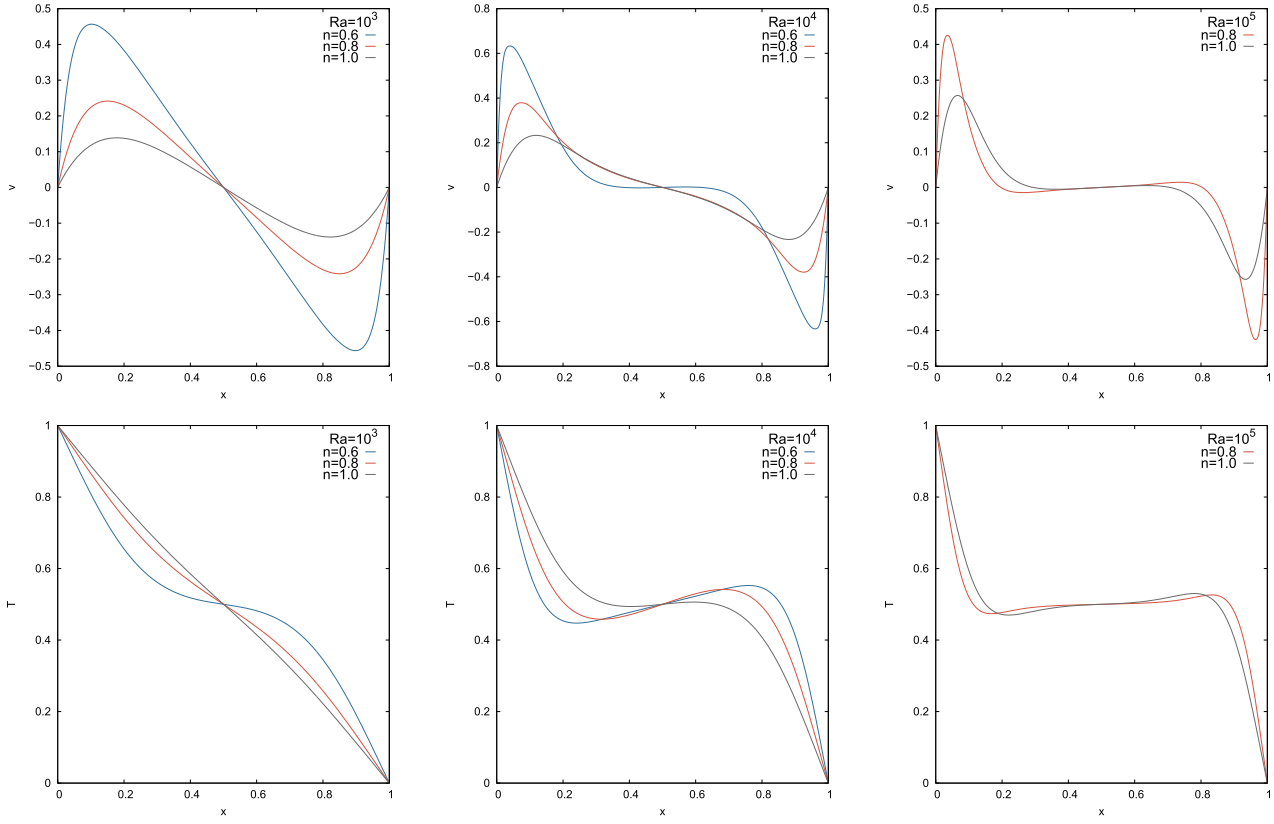


**Fig. 8.** $v$-velocity (top) and temperature (bottom) profiles along the horizontal centerline of the cavity.

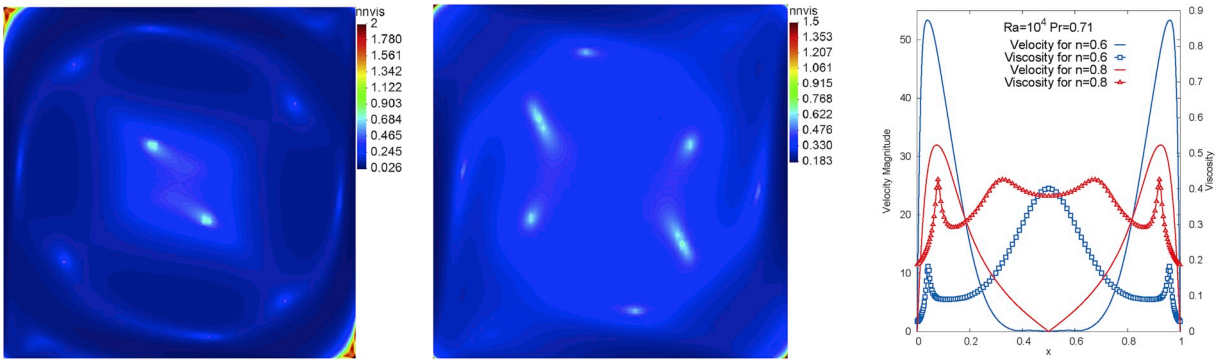


**Fig. 9.** Viscosity contour fill for $n = 0.6$ (left), $n = 0.8$ (center) and velocity magnitude-viscosity along the horizontal centerline of the cavity (right) for Ra = $10^4$.

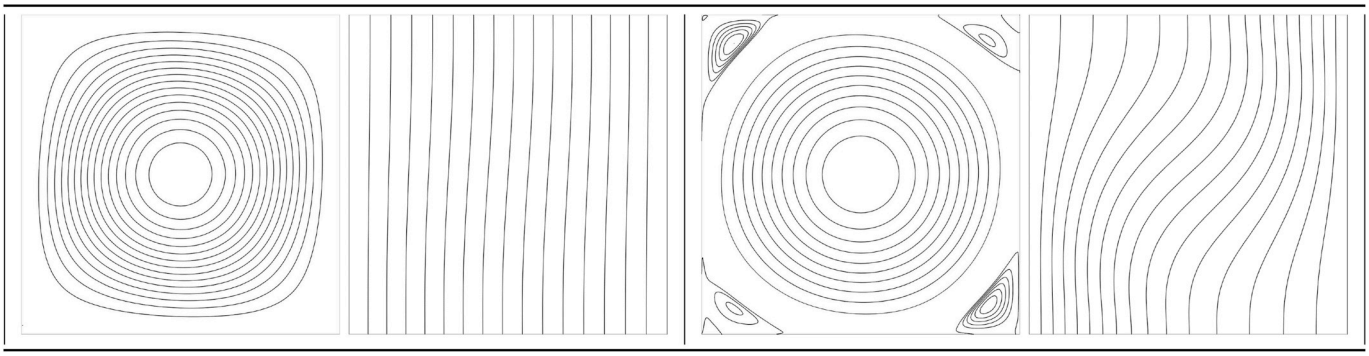

**Fig. 10.** Streamlines and isotherms for Pr = 0.01 and $n = 0.8$ at Ra = $10^2$ (left) and Ra = $10^3$ (right).

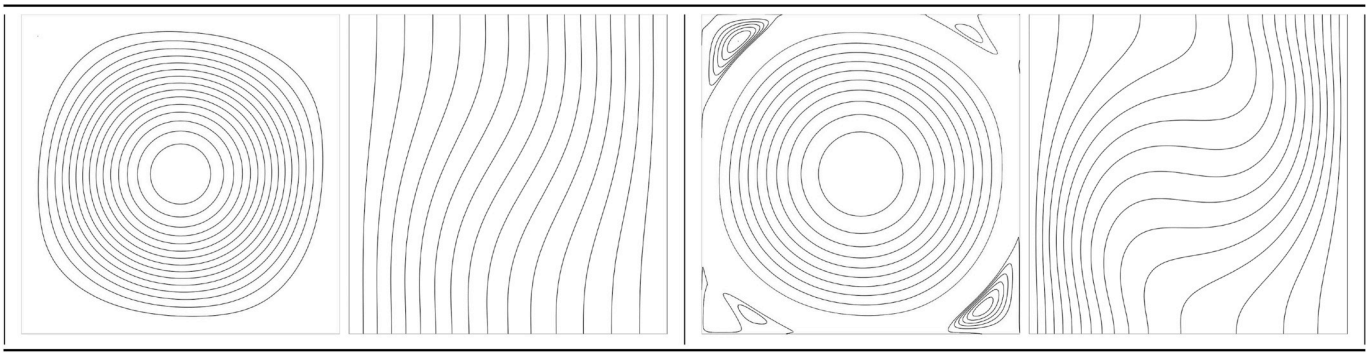

**Fig. 11.** Streamlines and isotherms for Pr = 0.01 and $n = 1.0$ at Ra = $10^3$ (left) and Ra = $10^4$ (right).

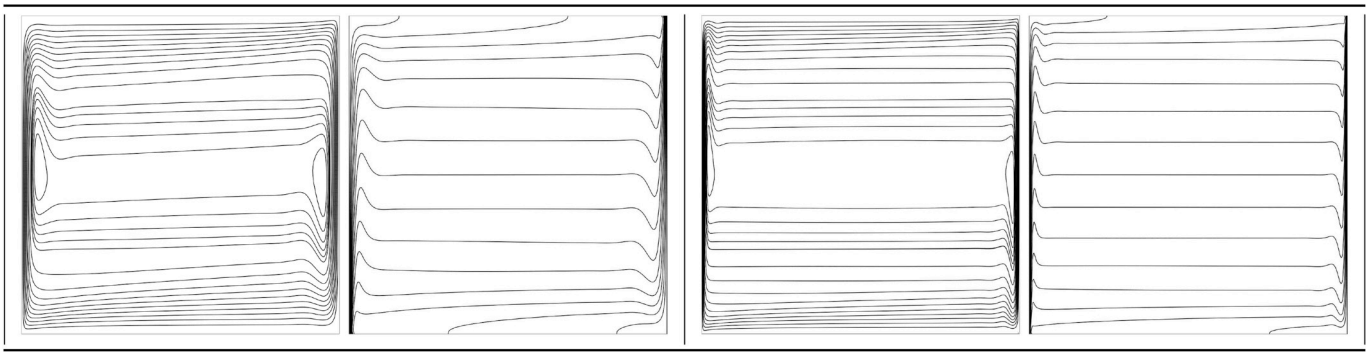

**Fig. 12.** Streamlines and isotherms for Pr = 1,000 and $n = 0.6$ at Ra = $10^6$ (left) and Ra = $10^7$ (right).

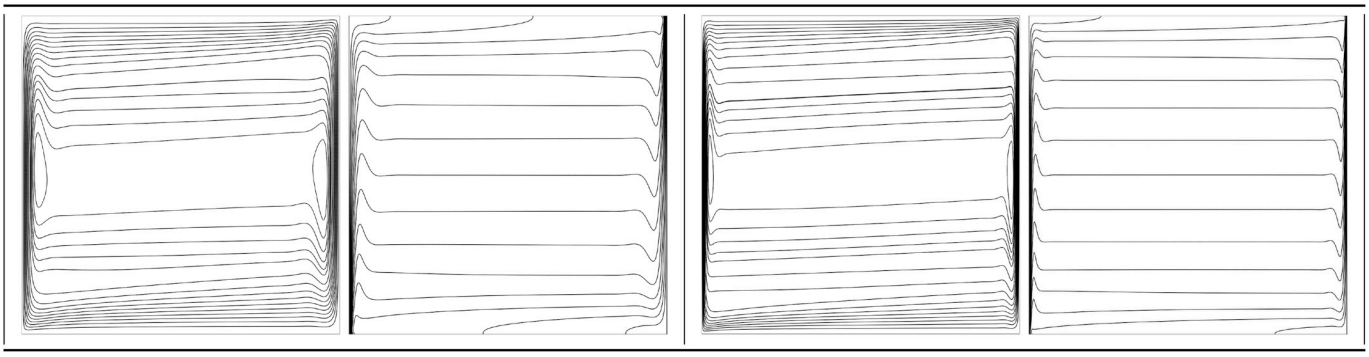

**Fig. 13.** Streamlines and isotherms for Pr = 1,000 and $n = 0.8$ at Ra = $10^7$ (left) and Ra = $10^8$ (right).

Regarding the time dependent dynamics, the oscillations appear in a similar fashion as in the Newtonian case presented in subsection 3.1, where the global solution seems steady but the small vortexes located close to the walls throbbe slightly at a fixed frequency. In the Pr = 0.71 case, the Hopf bifurcation takes place at a lower Ra for pseudoplastic fluids. Figs. 22 and 23 show streamlines, isotherms, Fourier frequency spectrum and phase diagram for time dependent cases.

In the Pr = 0.01 case, the Hopf bifurcations have been found at extremely low Ra compared to the Pr = 0.71 case. Likewise, for Pr = 1,000, the Hopf bifurcations have been found at extremely high Ra. Figs. 24 and 25 show the streamlines, isotherms, frequency spectrum and phase diagram of the first time dependent solution found in two of the cases. A notable characteristic of these cases is that for lower Pr and $n$, the Ra for which the problem turns globally oscillatory approaches to $Ra_c$, and determining the range where the Hopf bifurcation occurs requires a cautious search.

Lastly, it has been found that the fundamental frequencies increase following the same trend as the Hopf bifurcations found: as $n$ and Pr increase, the frequencies are higher. Table 7 summarizes the values that we have found for the first time dependent solutions in different cases, which are defined by the upper limit of the ranges presented in Table 6. For a fixed Pr value, the fundamental frequency value increases slightly with $n$; however, for a fixed $n$ there is a strong increase in the frequency values as Pr increases. It is important to note that the differences in their values depend also on the Rayleigh number value in which the bifurcation has been found, and the fact that the higher frequencies are

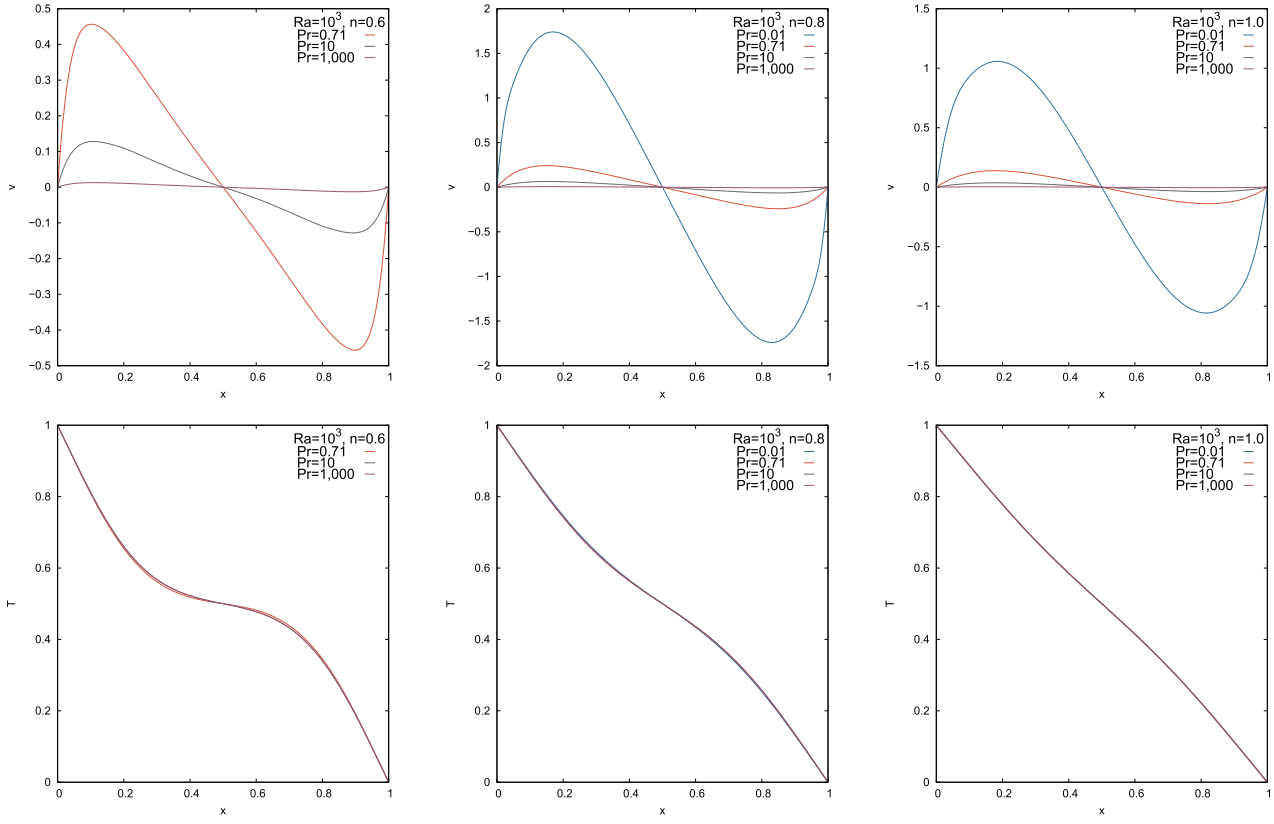


**Fig. 14.** $v$-velocity (top) and temperature (bottom) profiles along the horizontal centerline for different Pr at Ra = $10^3$.

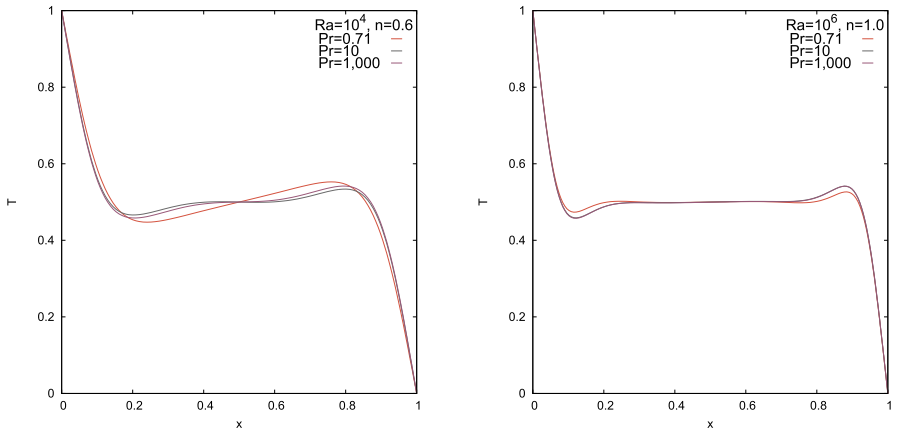


**Fig. 15.** Temperature profiles along the horizontal centerline for different Pr at Ra = $10^4$ (left) and Ra = $10^6$ (right).

found in the most convective cases.

### 3.6. Shell and tubes heat exchanger

In this subsection, a simplified shell and tubes heat exchanger is analyzed. Similar problems have been studied by many authors both numerically and experimentally, in order to improve the design and performance of these devices [37–40]; the design changes often include modifications on baffles [41,42] and arrangements of tubes [43]. However, in this work the heat exchange improvement is tested by using non-Newtonian fluids instead of modifying the exchanger geometry. The aim of this part of the work is to evaluate the enhancement of heat transfer using shear-thinning fluids in an applied problem. As a simplification, natural convection is not considered in the problem and, therefore, the heat transfer comes from purely forced convection. This implies that a possible Hopf bifurcation would depend only on Re, since Ra = 0, while for a mixed convection problem it would depend on both Re and Ra.

A 2D section of the computational domain is presented in Fig. 26. Note that all dimensions are relative to the entrance diameter D. No-slip conditions are set in all surfaces except for the entrance and exit of the shell, which are set to a fixed unitary inlet velocity and free traction, respectively. For the thermal boundary conditions, the walls and baffles are set as adiabatic, and the flow is assumed to enter the shell at a fixed cold temperature ($T_C = 0$). In order to focus the study on the heat exchange performance of non-Newtonian fluids that flow through the shell, the tubes are set with a fixed hot temperature ($T_H = 1$), which should be maintained by an isothermal internal fluid, for example.

The logarithmic mean temperature difference (LMTD) is a common tool used to calculate heat exchangers since it accurately describes the non-linear heat transfer that characterizes them [44]. We use it here to check the performance of the system for different power-law indexes.

For heat exchangers, the Reynolds number is computed differently depending on how the authors approach the problem. The main difference is how the hydraulic diameter is computed, which is usually a function of the shell diameter, the tube diameters, the number of tubes, transversal areas or any important geometric feature characteristic of the work of each author [37,45,46]. In our case, the Reynolds number is computed as described in Eq. (5), being $U$ the flow velocity at the entrance of the shell and using the diameter $D$ as the characteristic length. The Prandtl number, which is computed as described in Eq. (5), is reduced to the expression $|\mathrm{Pr}| = |m|$ and is set to a value equal to 5 for every case. As for the LMTD, it is computed as

$$\Delta T_{\mathrm{ml}} = \frac{\Delta T_1 - \Delta T_2}{\ln(\Delta T_1/\Delta T_2)} = \frac{\overline{T}_{\mathrm{out}} - T_C}{\ln\left(\frac{T_H - T_C}{T_H - \overline{T}_{\mathrm{out}}}\right)}, \tag{20}$$

where $\Delta T_1 = T_H - T_C$ and $\Delta T_2 = T_H - \overline{T}_{\mathrm{out}}$ are the temperature difference between the shell and the tubes in the entrance and the exit, respectively, and $\overline{T}_{\mathrm{out}}$ is the mean temperature at the exit of the shell side, computed as the average of a set of 9 points at the outlet surface.

For the numerical experiment, the problem is solved for Reynolds numbers up to Re = 700 for Newtonian and shear-thinning fluids, using power-law indexes $n$ = 0.5, 0.75, 1.0. All cases are solved using a mesh

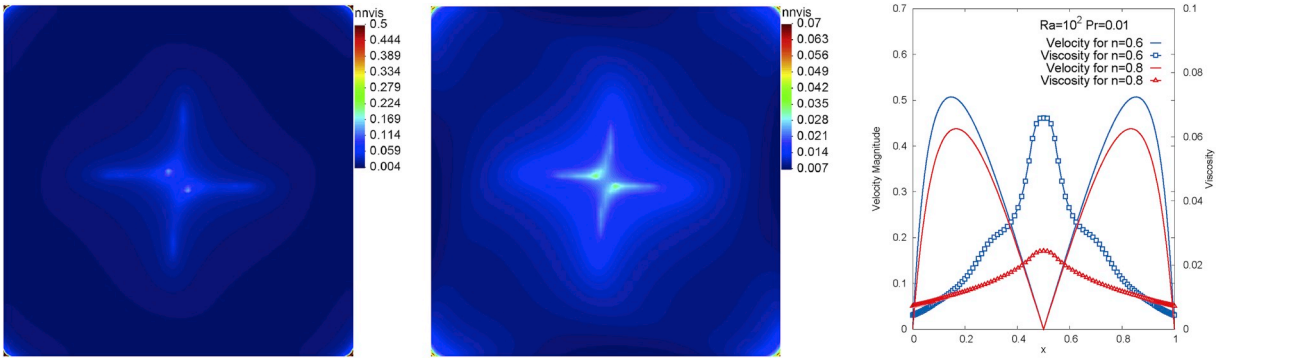


**Fig. 16.** Viscosity contour fill for $n$ = 0.6 (left), $n$ = 0.8 (center) and velocity magnitude-viscosity along the horizontal centerline of the cavity (right) for Ra = $10^2$ and Pr = 0.01.

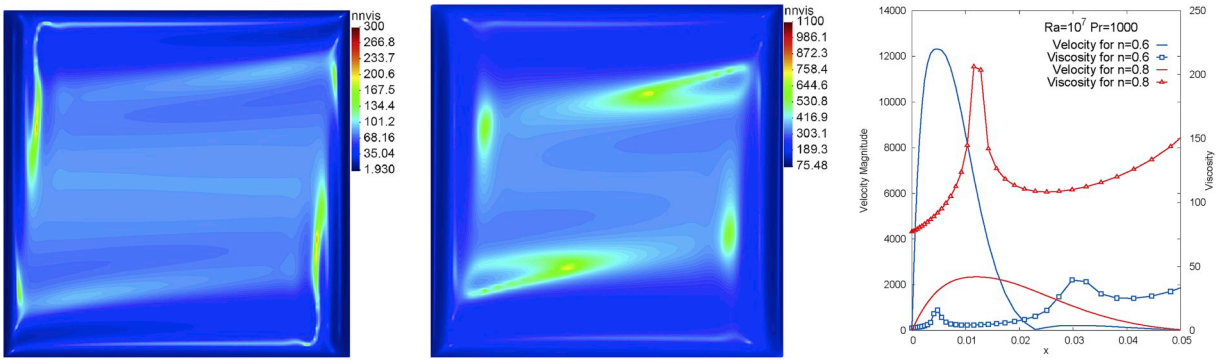


**Fig. 17.** Viscosity contour fill for $n = 0.6$ (left), $n = 0.8$ (center) and velocity magnitude-viscosity along the horizontal centerline of the cavity (right) for $Ra = 10^7$ and $Pr = 1{,}000$.

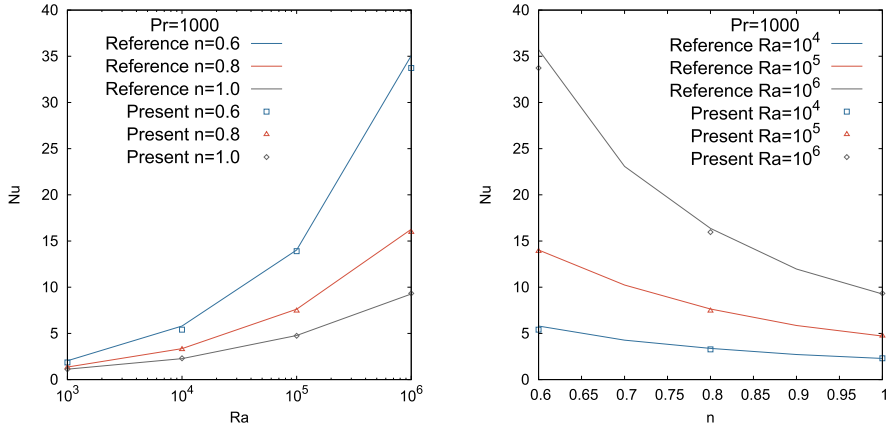


**Fig. 18.** Nusselt numbers for different Ra and $n$ for a fixed $Pr = 1{,}000$ compared with [20].

**Table 2**
Nusselt numbers at the hot wall for $Pr = 0.01$.

| | $n = 0.6$ | $n = 0.8$ | $n = 1.0$ |
|---|---|---|---|
| $Ra = 10^2$ | 1.0029 | 1.0018 | 1.0014 |
| $Ra = 10^3$ | – | 1.2500 | 1.1025 |
| $Ra = 10^4$ | – | – | 1.9569 |

**Table 3**
Nusselt numbers at the hot wall for $Pr = 0.71$.

| | $n = 0.6$ | $n = 0.8$ | $n = 1.0$ |
|---|---|---|---|
| $Ra = 10^2$ | 1.0030 | 1.0019 | 1.0014 |
| $Ra = 10^3$ | 1.8076 | 1.3161 | 1.1178 |
| $Ra = 10^4$ | 4.0817 | 2.9877 | 2.2450 |
| $Ra = 10^5$ | – | 6.1700 | 4.5226 |
| $Ra = 10^6$ | – | – | 8.8316 |
| $Ra = 10^7$ | – | – | 16.5498 |
| $Ra = 10^8$ | – | – | 30.3345 |

of 1,900,000 unstructured linear tetrahedral elements. Streamlines and isotherms in the case of $Re = 100$ and $n = 0.75$ are shown in Fig. 27 in order to show the heat exchanger dynamics.

A detailed view of a section through the entrance of the shell, perpendicular to the tubes, is presented in Fig. 28 for $n = 0.5$ cases, up to $Re = 700$. As seen in the velocity vectors through increasing Re, the flow evolves into a complex flow structure as the Reynolds number increases, being close to the entrance where the most complex dynamics take place. The last image in Fig. 28 is related to the viscosity contours associated to the $Re = 700$ case. In this image, it can be seen

**Table 4**
Nusselt numbers at the hot wall for $Pr = 10$.

| | $n = 0.6$ | $n = 0.8$ | $n = 1.0$ |
|---|---|---|---|
| $Ra = 10^2$ | 1.0030 | 1.0019 | 1.0014 |
| $Ra = 10^3$ | 1.8575 | 1.3175 | 1.1178 |
| $Ra = 10^4$ | 5.1394 | 3.2609 | 2.2748 |
| $Ra = 10^5$ | 12.0374 | 7.3844 | 2.8990 |
| $Ra = 10^6$ | – | 15.5922 | 9.2385 |
| $Ra = 10^7$ | – | 31.5550 | 17.3829 |
| $Ra = 10^8$ | – | – | 32.0212 |
| $Ra = 10^9$ | – | – | 58.4943 |
| $Ra = 10^{10}$ | – | – | 106.8007 |

**Table 5**
Nusselt numbers at the hot wall for $Pr = 1{,}000$.

| | $n = 0.6$ | $n = 0.8$ | $n = 1.0$ |
|---|---|---|---|
| $Ra = 10^2$ | 1.0030 | 1.0019 | 1.0014 |
| $Ra = 10^3$ | 1.8588 | 1.3174 | 1.1178 |
| $Ra = 10^4$ | 5.4069 | 3.2730 | 2.3083 |
| $Ra = 10^5$ | 13.9009 | 7.4460 | 4.7448 |
| $Ra = 10^6$ | 33.7299 | 15.9648 | 9.3339 |
| $Ra = 10^7$ | 79.3210 | 32.7635 | 17.6010 |
| $Ra = 10^8$ | – | 67.3876 | 32.5532 |
| $Ra = 10^9$ | – | – | 59.5297 |
| $Ra = 10^{10}$ | – | – | 108.0825 |
| $Ra = 10^{11}$ | – | – | 201.0267 |
| $Ra = 10^{12}$ | – | – | 377.8206 |

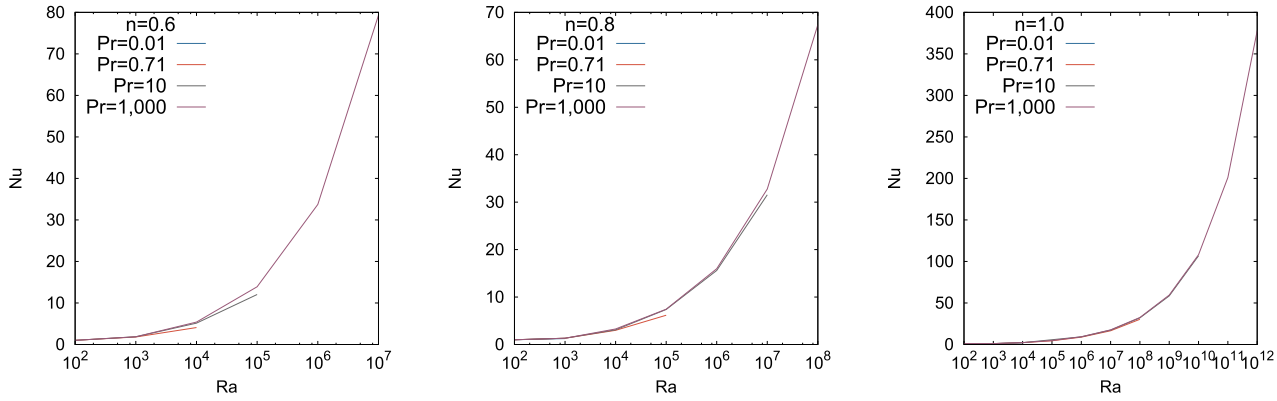


**Fig. 19.** Nusselt number for different $n$.

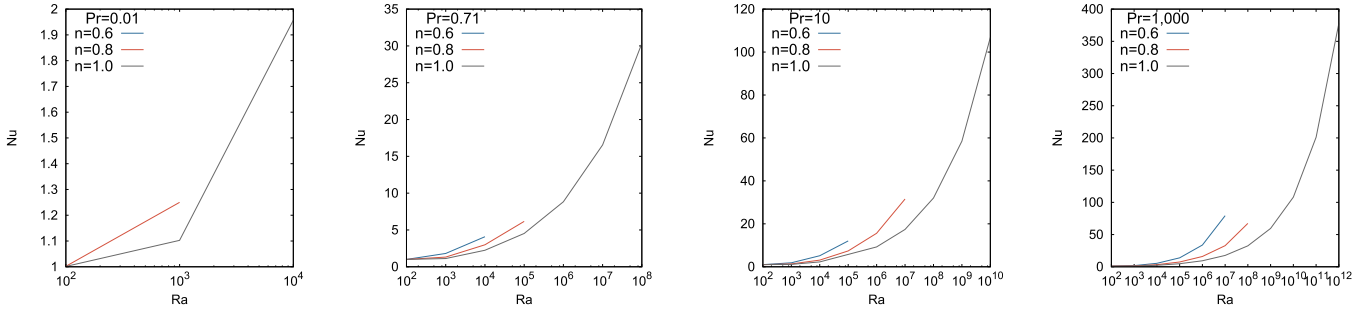


**Fig. 20.** Nusselt number for different Pr.

**Table 6**
Rayleigh number range where Hopf bifurcations has been found.

| | $n = 0.6$ | $n = 0.8$ | $n = 1.0$ |
|---|---|---|---|
| Pr = 0.01 | $5.00{\cdot}10^2 \lesssim \mathrm{Ra}_c \lesssim 5.25{\cdot}10^2$ | $2.50{\cdot}10^3 \lesssim \mathrm{Ra}_c \lesssim 2.75{\cdot}10^3$ | $2.25{\cdot}10^4 \lesssim \mathrm{Ra}_c \lesssim 5.00{\cdot}10^4$ |
| Pr = 0.71 | $2.50{\cdot}10^4 \lesssim \mathrm{Ra}_c \lesssim 2.75{\cdot}10^4$ | $5.50{\cdot}10^5 \lesssim \mathrm{Ra}_c \lesssim 6.00{\cdot}10^5$ | $1.70{\cdot}10^8 \lesssim \mathrm{Ra}_c \lesssim 1.71{\cdot}10^8$ |
| Pr = 10 | $4.75{\cdot}10^5 \lesssim \mathrm{Ra}_c \lesssim 4.85{\cdot}10^5$ | $1.55{\cdot}10^7 \lesssim \mathrm{Ra}_c \lesssim 1.6{\cdot}10^7$ | $2.25{\cdot}10^{10} \lesssim \mathrm{Ra}_c \lesssim 4.00{\cdot}10^{10}$ |
| Pr = 1,000 | $3.00{\cdot}10^7 \lesssim \mathrm{Ra}_c \lesssim 4.00{\cdot}10^7$ | $1.10{\cdot}10^9 \lesssim \mathrm{Ra}_c \lesssim 1.50{\cdot}10^9$ | $1.50{\cdot}10^{12} \lesssim \mathrm{Ra}_c \lesssim 2.50{\cdot}10^{12}$ |

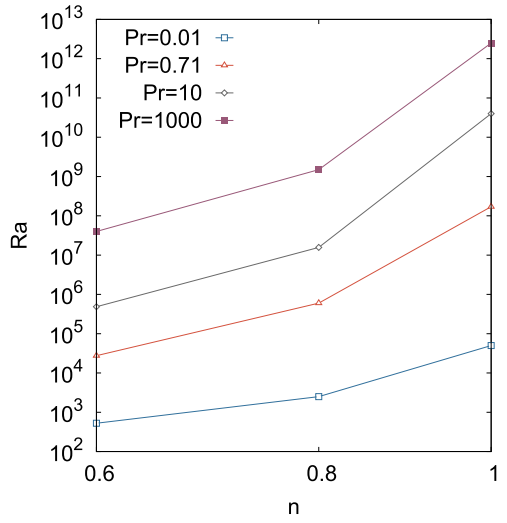


**Fig. 21.** $\mathrm{Ra}_c$ for different Pr and $n$.

that the lowest viscosity values are found in the zones where the velocity gradients are higher, as expected from the rheological point of view. As for the $n = 0.75$ cases, the flow evolve similarly but less pronounced shear-thinning dynamics.

The numerical values of the LMTD in each case are presented in Table 8. The LMTD decreases for lower $n$ and Re values, which means that the cold fluid heats in a shorter length through the shell, proving that the heat exchange is stronger when using shear-thinning fluids for a fixed Re at the same flow conditions.

By analyzing the relative difference of the results reported in Table 8, the heat transfer enhancement due to the LMTD improvement obtained by using a pseudoplastic fluid instead of a Newtonian fluid goes from 27.9% at the lowest Reynolds number using $n = 0.75$, to 44.1% at the highest Reynolds number using $n = 0.5$ of the studied cases. Regarding the time dependent behavior of the problem, there was no sign of flow instabilities in the range of physical parameters studied.

## 4. Conclusion

In this work, a VMS finite element formulation has been used in the thermally coupled cavity flow problem to validate existing results of

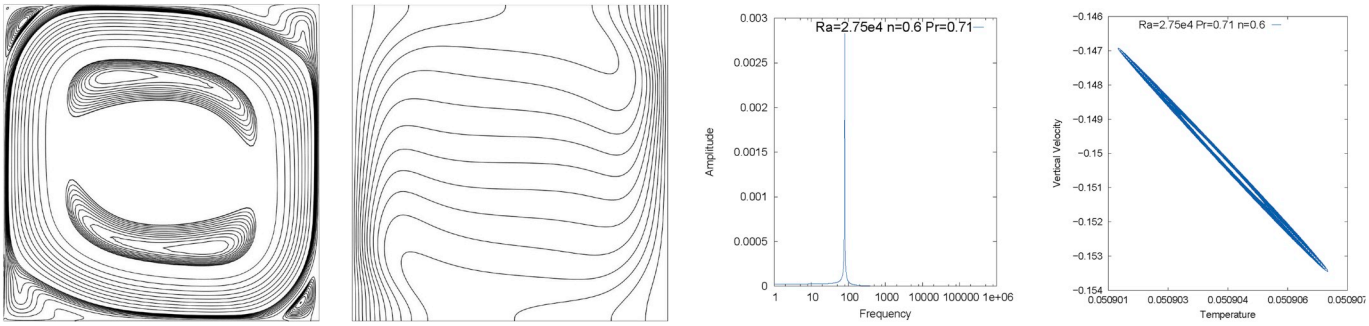


**Fig. 22.** From left to right: Streamlines and isotherms for Ra = $2.75 \cdot 10^4$, Pr = 0.71, $n$ = 0.6, Fourier frequency spectrum and phase diagram at coordinates (0.19, 0.01).

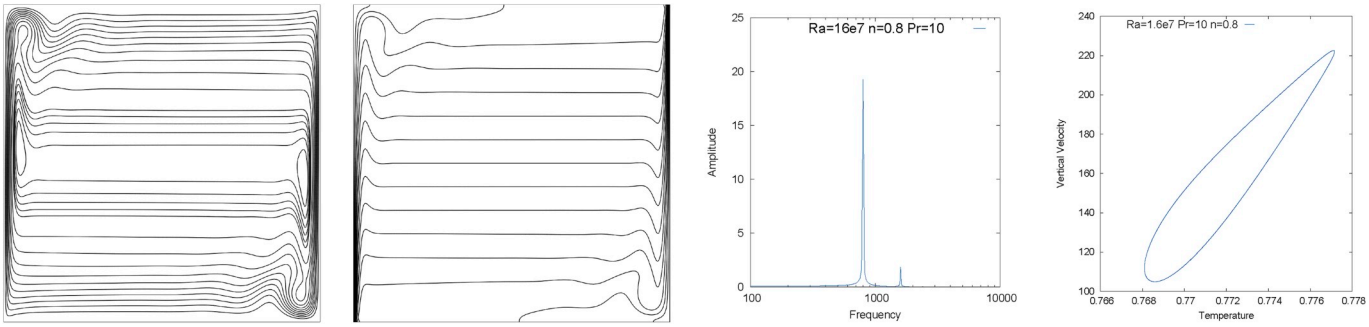


**Fig. 23.** From left to right: Streamlines and isotherms for Ra = $1.6 \cdot 10^7$, Pr = 10, $n$ = 0.8, Fourier frequency spectrum and phase diagram at coordinates (0.06, 0.92).

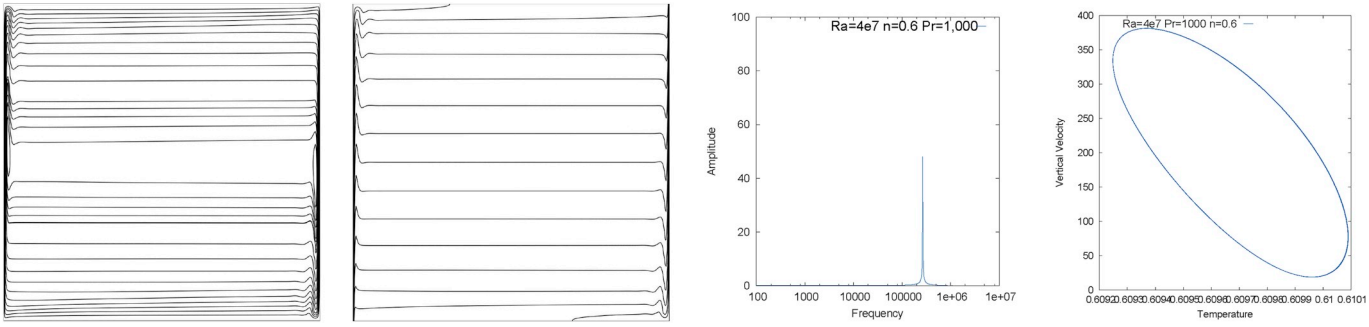


**Fig. 24.** From left to right: Streamlines and isotherms for Ra = $4 \cdot 10^7$, Pr = 1,000, $n$ = 0.6, Fourier frequency spectrum and phase diagram at coordinates (0.5, 0.01).

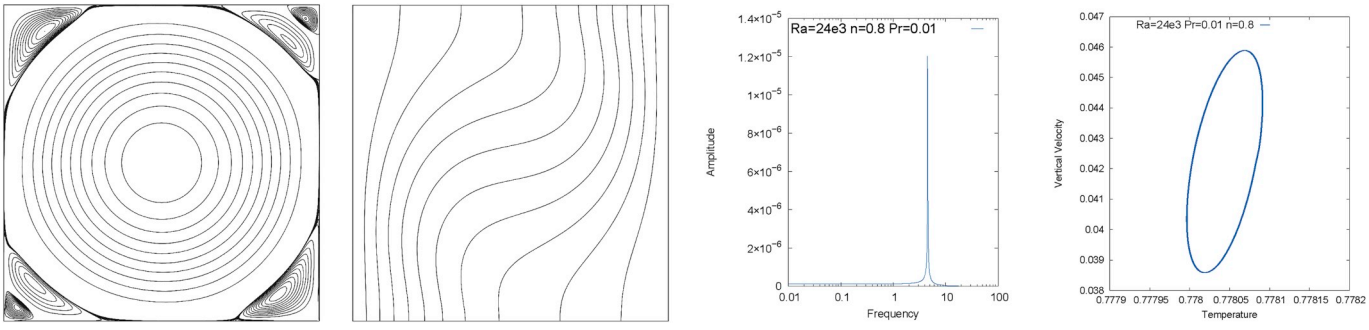


**Fig. 25.** From left to right: Streamlines and isotherms for Ra = $2.4 \cdot 10^3$, Pr = 0.01, $n$ = 0.8, Fourier frequency spectrum and phase diagram at coordinates (0.26, 0.29).

**Table 7**
Fundamental frequencies of the first time dependent solution.

| | $n$ = 0.6 | $n$ = 0.8 | $n$ = 1.0 |
|---|---|---|---|
| Pr = 0.01 | 3.2 | 4.53 | 16.2 |
| Pr = 0.71 | 82.5 | 255 | 6500 |
| Pr = 10 | 700 | 798 | 28000 |
| Pr = 1,000 | 265000 | 671900 | 7099000 |

Newtonian and non-Newtonian fluid flows found in the literature. The formulation has proved to be robust enough to compute high Rayleigh number flows of power-law fluids accurately.

The buoyancy driven flow has been analyzed using both Newtonian and non-Newtonian fluids, in order to understand the influence of $n$ and Pr in the flow dynamics and its thermal capabilities at high Ra. It has been found that, in comparison to Newtonian fluids, shear-thinning fluids have improved heat transfer capabilities for a fixed Ra and Pr,

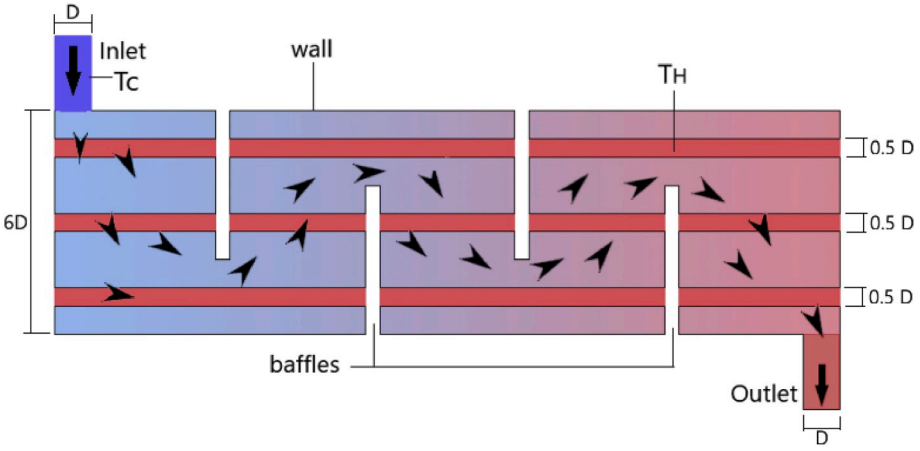


**Fig. 26.** Computational domain.

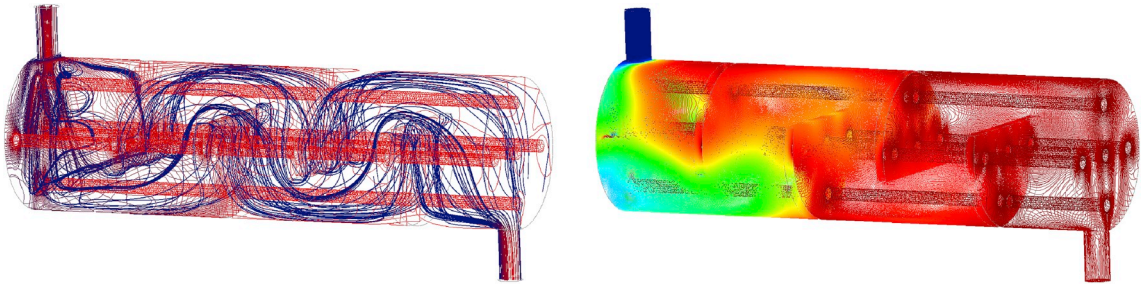

**Fig. 27.** 3D Streamlines and isotherms for $n = 0.75$ and Re = 100.

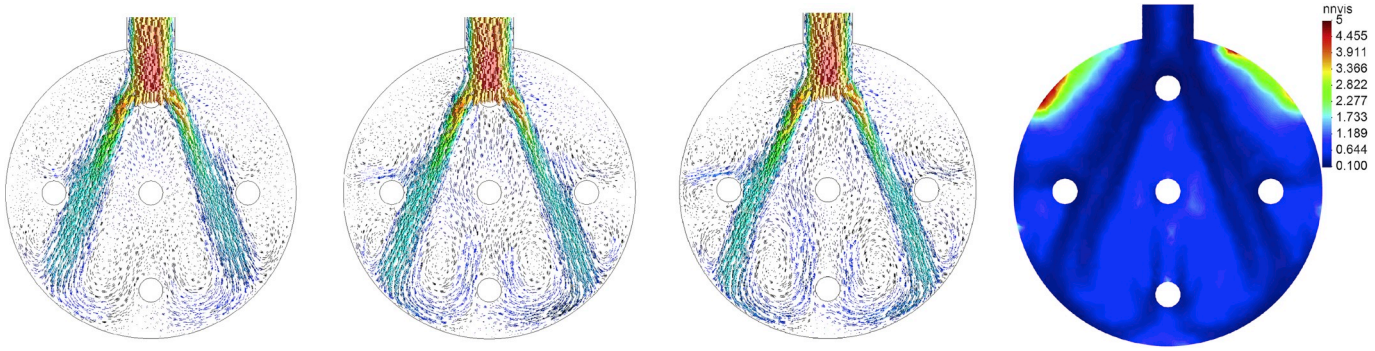


**Fig. 28.** Inlet cut plane of $n = 0.5$ cases, from left to right: velocity vectors for Re = 300, 500, 700 and viscosity contours for Re = 700.

**Table 8**
Logarithmic mean temperature difference for Re = 100,300,500,700 and $n = 0.5, 0.75, 1$.

| | Re = 100 | Re = 300 | Re = 500 | Re = 700 |
|---|---|---|---|---|
| $n = 0.5$ | 0.23443566 | 0.35446767 | 0.38151896 | 0.39809371 |
| $n = 0.75$ | 0.37171724 | 0.46817087 | 0.49013614 | 0.51338056 |
| $n = 1.0$ | 0.52324019 | 0.56642185 | 0.62668311 | 0.71269488 |

and they also improve by increasing Ra independently of the fluid type. The power-law index has also a great influence in the critical value of Ra ($Ra_c$) that defines when the time dependent behavior starts; it has been found that the Hopf bifurcation appears later as both $n$ and Pr increase independently. As for the effect of Pr, it has been proved that it has little influence on the Nusselt number but it greatly delays the development of the flow. The influence of $n$ and Pr is strong in the flow dynamics, and the $Ra_c$ for which the Hopf bifurcation occurs can drastically change depending on their values.

Regarding the simplified heat exchanger example, significant improvements have been found regarding the enhancement of heat transfer using shear-thinning fluids compared with their Newtonian counterpart, opening the door for more complex and realistic future studies.

As a summary, this work intends to contribute with extensive information to understand the thermal behavior of non-Newtonian fluids, both in steady state flows and in the transition to time dependent flows through flow instabilities.

## Acknowledgments

This work has been partially funded by the Chilean Council for Scientific and Technological Research (CONICYT-FONDECYT 11160160). We also acknowledge the support received by the Scientific Research Projects Management Department of the Vice Presidency Research, Development and Innovation (DICYT-VRIDEI) at Universidad de Santiago de Chile in Proyecto Basal USA 1555 - Vridei 051716CSSSA-PUBLIC. Joan Baiges acknowledges the support of the Spanish Government through Ramón y Cajal grant RYC-2015-17367. R. Codina acknowledges the support received through the ICREA Academic Research Program.

## Appendix A

In Algorithm Appendix A, non-linear and global iterations are needed. Note that using this procedure, segregation errors are avoided, which is important when searching the critical values of the dimensionless numbers that yield Hopf bifurcations. If we denote with a double superscript the time step (j) and iteration counter (i), then we can solve the problem at time step $j+1$and to find the $i+1$ iteration of the unknowns; however, in our case a third superscript k that takes into account the global convergence of the problem is needed. Therefore, the unknowns velocity and pressure are defined by $\boldsymbol{u}_h^{j+1,k+1,i+1}$ and $p_h^{j+1,k+1,i+1}$, respectively, while the temperature unknown is, $T_h^{j+1,k+1}$ as the energy equation is linear in the temperature for a given velocity. The k counter ensures global convergence between the three unknown fields, and thus, the temporal error is that of the time scheme integrator (Eq. (13)). The superscripts in the stabilization parameters, the viscosity and the residuals (for the momentum equation $\boldsymbol{R}_u$ and for the energy equation $R_T$) correspond to those of the variables with which they have been computed.

---

**Algorithm 1** Decoupling in time algorithm.

**For each time step** $j+1$ **do:**

**Global Step** (global loop, $k$ counter):

**Known data:** $\boldsymbol{u}_h^{j-1}$, $\boldsymbol{u}_h^{j}$, $\boldsymbol{u}_h^{j+1,k}$, $p_h^{j+1,k}$ and $T_h^{j+1,k}$

**First step (non-linear loop):** Solve the Navier-Stokes equations for a known body force term.

**Known data:** $u_h^{j+1,k+1,i}$, $p_h^{j+1,k+1,i}$

$$\rho\left(\frac{3\boldsymbol{u}_h^{j+1,k+1,i+1}}{2\delta t},\boldsymbol{v}_h\right)+\langle\rho\boldsymbol{u}_h^{j+1,k+1,i}.\nabla\boldsymbol{u}_h^{j+1,k+1,i+1},\boldsymbol{v}_h\rangle-(p_h^{j+1,k+1,i+1},\nabla\cdot\boldsymbol{v}_h)$$

$$+\langle 2\eta^{j+1,k+1,i}\nabla^s\boldsymbol{u}_h^{j+1,k+1,i+1},\nabla^s\boldsymbol{v}_h\rangle+\sum_K\alpha_2^{j+1,k+1,i}\langle\nabla\cdot\boldsymbol{u}_h^{j+1,k+1,i+1},\nabla\cdot\boldsymbol{v}_h\rangle_K$$

$$+\sum_K\alpha_1^{j+1,k+1,i}\langle\boldsymbol{R}_u^{j+1,k+1,i+1},-\rho\boldsymbol{u}_h^{j+1,k+1,i}.\nabla\boldsymbol{v}_h-\nabla\cdot(2\eta^{j+1,k+1,i}\nabla^s\boldsymbol{v}_h)\rangle=\langle\rho\boldsymbol{g}\beta(T_h^{j+1,k}-T_{\mathrm{ref}}),\boldsymbol{v}_h\rangle$$

$$+\rho\left(\frac{4\boldsymbol{u}_h^{j}-\boldsymbol{u}_h^{j-1}}{2\delta t},\boldsymbol{v}_h\right),$$

$$(\nabla\cdot\boldsymbol{u}_h^{j+1,k+1,i+1},q_h)+\sum_K\alpha_1^{j+1,k+1,i}\langle\boldsymbol{R}_u^{j+1,k+1,i+1},-\nabla q_h\rangle=0,$$

**Check convergence between:** Velocity ($\boldsymbol{u}_h^{j+1,k+1,i}$ and $\boldsymbol{u}_h^{j+1,k+1,i+1}$) and pressure ($p_h^{j+1,k+1,i}$ and $p_h^{j+1,k+1,i+1}$)

**Set:** $u_h^{j+1,k+1}:=u_h^{j+1,k+1,i+1}$ and $p_h^{j+1,k+1}:=p_h^{j+1,k+1,i+1}$

**Second Step:** Solve the energy equation using the velocity obtained in step 1.

$$\rho c_p\left(\frac{3T_h^{j+1,k+1}}{2\delta t},\Theta_h\right)+\langle\rho c_p\boldsymbol{u}_h^{j+1,k+1}.\nabla T_h^{j+1,k+1},\Theta_h\rangle+k(\nabla T_h^{j+1,k+1},\nabla\Theta_h)$$

$$+\sum_K\alpha_3^{j+1,k+1}\langle R_T^{j+1,k+1},-\rho c_p\boldsymbol{u}_h^{j+1,k+1}.\nabla\Theta_h-k\Delta\Theta_h\rangle_K=\rho c_p\left(\frac{4T_h^{j}-T_h^{j-1}}{2\delta t},\Theta_h\right),$$

**Check convergence between:** Velocity ($\boldsymbol{u}_h^{j+1,k}$ and $\boldsymbol{u}_h^{j+1,k+1}$), pressure ($p_h^{j+1,k}$ and $p_h^{j+1,k+1}$) and temperature ($T_h^{j+1,k}$ and **Error! Not a valid embedded object.**)

**Set:** $u_h^{j+1}=u_h^{j+1,k+1}$, $p_h^{j+1}=p_h^{j+1,k+1}$ and $T_h^{j+1}=T_h^{j+1,k+1}$

---

## Appendix B. Supplementary data

Supplementary data to this article can be found online at https://doi.org/10.1016/j.ijthermalsci.2019.106022.

## References

[1] P.A. Cordoba, N. Silin, E.A. Dari, Natural convection in a cubical cavity filled with a fluid showing temperature-dependent viscosity, Int. J. Therm. Sci. 98 (2015) 255–265.
[2] M.M. El-Gendi, Numerical simulation of unsteady natural convection flow inside a pattern of connected open square cavities, Int. J. Therm. Sci. 127 (2018) 373–383.
[3] M. Dastmalchi, G. Sheikhzadeh, A.A. Arani, Double-diffusive natural convective in a porous square enclosure filled with nanofluid, Int. J. Therm. Sci. 95 (2015) 88–98.
[4] I. Miroshnichenko, M. Sheremet, Turbulent natural convection heat transfer in rectangular enclosures using experimental and numerical approaches: a review, Renew. Sustain. Energy Rev. 82 (2018) 40–59.
[5] M. Cruchaga, D. Celentano, Modelling ice melting processes: numerical and experimental validation, Int. J. Numer. Methods Heat Fluid Flow 17 (5) (2007) 548–564.
[6] M.A. Cruchaga, D.J. Celentano, A fixed-mesh finite element thermally coupled flow formulation for the numerical analysis of melting processes, Int. J. Numer. Methods Eng. 51 (10) (2001) 1231–1258.
[7] C. Nonino, G. Croce, An equal-order velocity-pressure algorithm for incompressible thermal flows, part 2: validation, Numer. Heat Transf. 32 (1) (1997) 17–35.
[8] C. Zhuo, C. Zhong, LES-based filter-matrix Lattice Boltzmann model for simulating turbulent natural convection in a square cavity, Int. J. Heat Fluid Flow 42 (2013) 10–22.
[9] E. Bucchignani, An implicit unsteady finite volume formulation for natural convection in a square cavity, Fluid Dyn. Mater. Process. 5 (1) (2009) 37–59.
[10] S. Xin, P.L. Quéré, Natural-convection flows in air-filled, differentially heated cavities with adiabatic horizontal walls, Numer. Heat Transf., Part A: Applications 50 (5) (2006) 437–466.
[11] H. Dixit, V. Babu, Simulation of high Rayleigh number natural convection in a square cavity using the Lattice Boltzmann method, Int. J. Heat Mass Transf. 49 (3) (2006) 727–739.
[12] G. Barakos, E. Mitsoulis, D. Assimacopoulos, Natural convection flow in a square cavity revisited: laminar and turbulent models with wall functions, Int. J. Numer. Methods Fluids 18 (7) (1994) 695–719.
[13] S. Xin, P. Le Quere, Direct numerical simulations of two-dimensional chaotic natural convection in a differentially heated cavity of aspect ratio 4, J. Fluid Mech. 304 (1995) 87–118.
[14] S. Parvin, R. Nasrin, M. Alim, Heat transfer performance of nanofluid in a complicated cavity due to Prandtl number variation, Procedia Eng. 90 (2014) 377–382 10th International Conference on Mechanical Engineering, ICME 2013.
[15] K.M. Gangawane, Computational analysis of mixed convection heat transfer characteristics in lid-driven cavity containing triangular block with constant heat flux: effect of Prandtl and Grashof numbers, Int. J. Heat Mass Transf. 105 (2017) 34–57.

[16] J. Ma, F. Xu, S.C. Saha, Flows and heat transfer of the transition to an unsteady state in a finned cavity for different Prandtl numbers, Int. Commun. Heat Mass Transf. 88 (2017) 220–227.
[17] P. Le Quéré, M. Behnia, From onset of unsteadiness to chaos in a differentially heated cavity, J. Fluid Mech. 359 (03 1998) 81–107.
[18] X. Wang, Y. Wei, X. Shen, Numerical investigation of the first bifurcation for natural convection of fluids enclosed in a 2d square cavity with Pr lower than 1.0, Energy Convers. Manag. 50 (10) (2009) 2504–2512.
[19] B. Zhao, Z. Tian, High-resolution high-order upwind compact scheme-based numerical computation of natural convection flows in a square cavity, Int. J. Heat Mass Transf. 98 (2016) 313–328.
[20] O. Turan, A. Sachdeva, N. Chakraborty, R.J. Poole, Laminar natural convection of power-law fluids in a square enclosure with differentially heated side walls subjected to constant temperatures, J. Non-Newtonian Fluid Mech. 166 (17) (2011) 1049–1063.
[21] G.B. Kim, J.M. Hyun, H.S. Kwak, Transient buoyant convection of a power-law non-Newtonian fluid in an enclosure, Int. J. Heat Mass Transf. 46 (19) (2003) 3605–3617.
[22] N.O. Moraga, E.F. Castillo, C.P. Garrido, Non Newtonian annular alloy solidification in mould, Heat Mass Transf. 48 (Aug 2012) 1415–1424.
[23] P. Ternik, R. Rudolf, Laminar natural convection of non-Newtonian nanofluids in a square enclosure with differentially heated side walls, Int. J. Simul. Model. 12 (1) (2013) 5–16.
[24] A. Aguirre, E. Castillo, M. Cruchaga, R. Codina, J. Baiges, Stationary and time-dependent numerical approximation of the lid-driven cavity problem for power-law fluid flows at high Reynolds numbers using a stabilized finite element formulation of the VMS type, J. Non-Newtonian Fluid Mech. 257 (2018) 22–43.
[25] R.P. Chhabra, J.F. Richardson, Non-Newtonian Flow and Applied Rheology, second ed., Elsevier Butterworth-Heinemann, 2008.
[26] R.B. Bird, W.E. Stewart, E.N. Lightfoot, Transport Phenomena, second ed., Wiley, New York, 2002.
[27] E. Castillo, R. Codina, Stabilized stress-velocity-pressure finite element formulations of the Navier-Stokes problem for fluids with non-linear viscosity, Comput. Methods Appl. Mech. Eng. 279 (2014) 554–578.
[28] E. Castillo, R. Codina, Variational multi-scale stabilized formulations for the stationary three-field incompressible viscoelastic flow problem, Comput. Methods Appl. Mech. Eng. 279 (2014) 579–605.
[29] T.J. Hughes, G.R. Feijóo, L. Mazzei, J.-B. Quincy, The variational multiscale method-a paradigm for computational mechanics, Comput. Methods Appl. Mech. Eng. 166 (1–2) (1998) 3–24.
[30] R. Codina, J. Principe, M. Ávila, Finite Element approximation of turbulent thermally coupled incompressible flows with numerical sub-grid scale modelling, Int. J. Numer. Methods Heat Fluid Flow 20 (5) (2010) 492–516.
[31] R. Codina, J. Principe, Dynamic subscales in the finite element approximation of thermally coupled incompressible flows, Int. J. Numer. Methods Fluids 54 (6–8) (2007) 707–730.
[32] R. Codina, S. Badia, J. Baiges, J. Principe, Variational multiscale methods in computational fluid dynamics, Encyclopedia of Computational Mechanics, John Wiley & Sons Ltd., 2018, pp. 1–28.
[33] E. Castillo, R. Codina, Finite element approximation of the viscoelastic flow problem: a non-residual based stabilized formulation, Comput. Fluids 142 (2017) 72–78 Selected papers of 18th International Conference on Finite Elements in Flow Problems.
[34] E. Castillo, R. Codina, Dynamic term-by-term stabilized finite element formulation using orthogonal subgrid-scales for the incompressible navier-stokes problem, Comput. Methods Appl. Mech. Eng. 349 (1) (2019) 701–721.
[35] F. Arpino, N. Massarotti, A. Mauro, High Rayleigh number laminar-free convection in cavities: new benchmark solutions, Numer. Heat Transf., Part B: Fundamentals 58 (2) (2010) 73–97.
[36] P.X. Yu, Z.F. Tian, Compact computations based on a stream-function–velocity formulation of two-dimensional steady laminar natural convection in a square cavity, Phys. Rev. E 85 (3) (2012) 036703.
[37] M. Mirzaei, H. Hajabdollahi, H. Fadakar, Multi-objective optimization of shell-and-tube heat exchanger by constructal theory, Appl. Therm. Eng. 125 (Supplement C) (2017) 9–19.
[38] B.I. Master, K.S. Chunangad, A.J. Boxma, D. Kral, P. Stehlík, Most frequently used heat exchangers from pioneering research to worldwide applications, Heat Transf. Eng. 27 (6) (2006) 4–11.
[39] Q. Wang, G. Chen, Q. Chen, M. Zeng, Review of improvements on shell-and-tube heat exchangers with helical baffles, Heat Transf. Eng. 31 (10) (2010) 836–853.
[40] P. Stehlík, V.V. Wadekar, Different strategies to improve industrial heat exchange, Heat Transf. Eng. 23 (6) (2002) 36–48.
[41] M. Mellal, R. Benzeguir, D. Sahel, H. Ameur, Hydro-thermal shell-side performance evaluation of a shell and tube heat exchanger under different baffle arrangement and orientation, Int. J. Therm. Sci. 121 (Supplement C) (2017) 138–149.
[42] Y. Lei, Y. Li, S. Jing, C. Song, Y. Lyu, F. Wang, Design and performance analysis of the novel shell-and-tube heat exchangers with louver baffles, Appl. Therm. Eng. 125 (Supplement C) (2017) 870–879.
[43] O. Labbadlia, B. Laribi, B. Chetti, P. Hendrick, Numerical study of the influence of tube arrangement on the flow distribution in the header of shell and tube heat exchangers, Appl. Therm. Eng. 126 (Supplement C) (2017) 315–321.
[44] M. Nitsche, R. Gbadamosi, Chapter 2 - calculations of the temperature differences lmtd and cmtd, in: M. Nitsche, R. Gbadamosi (Eds.), Heat Exchanger Design Guide, Butterworth-Heinemann, Boston, 2016, pp. 21–35.
[45] A.A. Tahery, S. Khalilarya, S. Jafarmadar, Effectively designed ntw shell-tube heat exchangers with segmental baffles using flow hydraulic network method, Appl. Therm. Eng. 120 (2017) 635–644.
[46] B. Gao, Q. Bi, Z. Nie, J. Wu, Experimental study of effects of baffle helix angle on shell-side performance of shell-and-tube heat exchangers with discontinuous helical baffles, Exp. Therm. Fluid Sci. 68 (2015) 48–57.